Czech Technical University in Prague
Faculty of Nuclear Sciences and Physical Engineering
Department of Physics

Diploma Thesis

Dependence of reconstructed kinematic characteristics of Z boson on the uncertainty of E-p scale in experiment ATLAS

Prague, 2008 **Michal Svatoš**

Supervisor: RNDr. Pavel Staroba, CSc., Institute of Physics of the Academy of Sciences of the Czech Republic, Prague, v.v.i.

Název práce:
Závislost rekonstruovaných kinematických charakteristik bosonu Z na neurčitosti energetické a impulsové škály v experimentu ATLAS

Autor: Michal Svatoš

Obor: Jaderné inženýrství

Druh práce: Diplomová práce

Vedoucí práce: RNDr. Pavel Staroba, CSc., FzÚ, AV ČR, v.v.i.

Konzultant: —

Abstrakt: Tato práce je rozdělena na dvě části. První je věnována popisu experimentu ATLAS. Zabývá se složením celého zařízení i funkcí jeho jednotlivých částí a některými jejich vlastnostmi. Stručně je popsáno i určení E-p škály a rekonstrukce a identifikace elektronů a fotonů v experimentu ATLAS. Druhá část ukazuje výsledky zkoumání vlivu neurčitosti E-p škály na hmotnost, hybnost a rapiditu Z bosonu.

Klíčová slova: Experiment ATLAS, E-p škála, Z boson, detektor částic, energetické a impulsové rozlišení

Title:
Dependence of reconstructed kinematic characteristics of Z boson on the uncertainty of E-p scale in experiment ATLAS

Author: Michal Svatoš

Abstract: This project is divided into two parts. The first one is dedicated to description of the experiment ATLAS. It deals with its overall functioning, function of its parts and some of their properties. Determination of E-p scale and electron and photon reconstruction and identification in the ATLAS detector are also briefly mentioned. The second part shows a results of investigation of influence of uncertainty of E-p scale on mass, momentum and rapidity of Z boson.

Key words: experiment ATLAS, E-p scale, Z boson, particle detector, energetic and momentum resolution

Contents

Part I

The ATLAS experiment

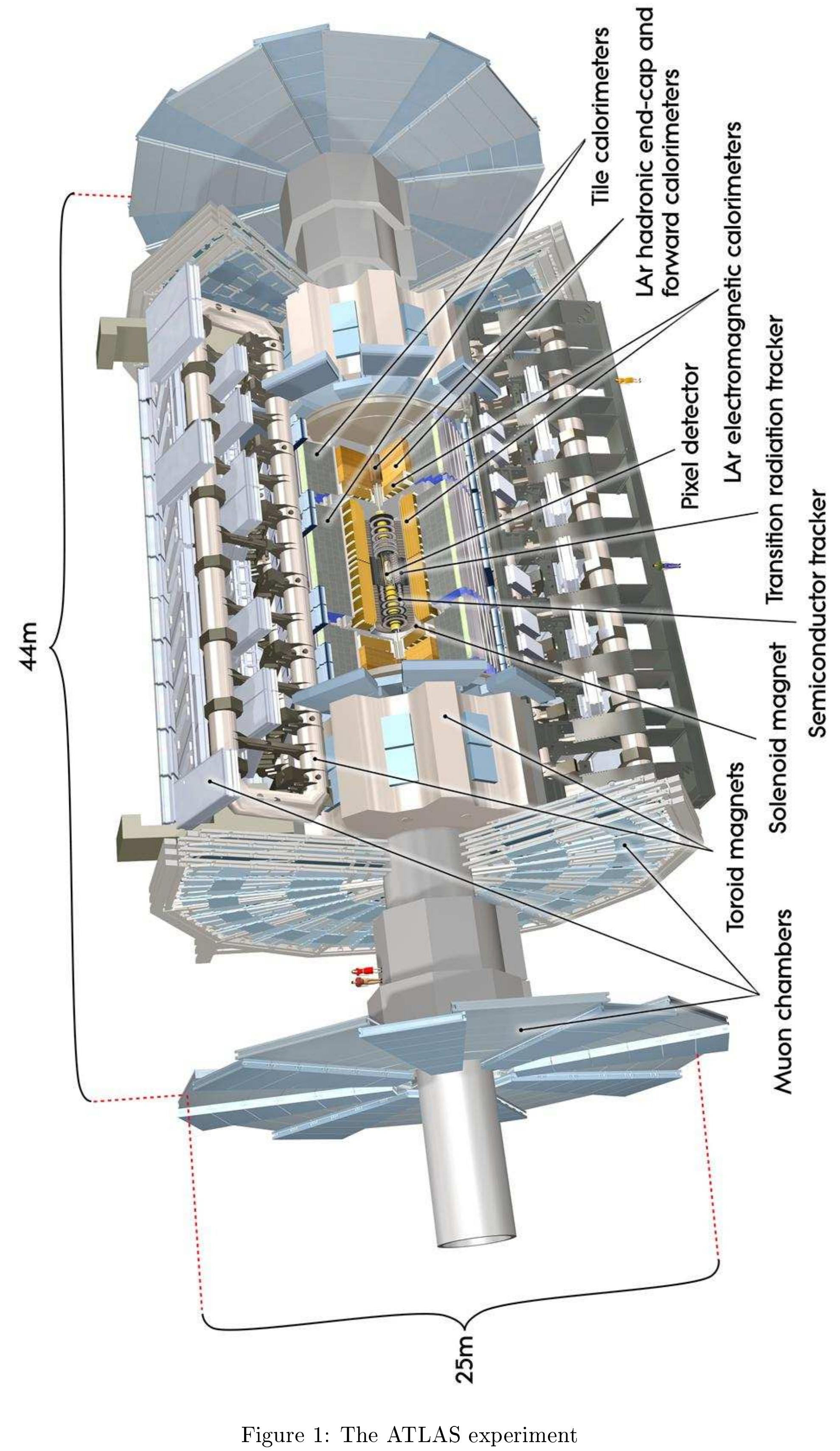

Figure 1: The ATLAS experiment

Chapter 1

Introduction

The LHC accelerator and experiments located there allow us to extend our knowledge of elementary particle physics. This can be achieved either by more accurate measurements of known objects of particle physics or by discovering new objects.

The ATLAS experiment is one of four large experiments located at LHC accelerator. It is depicted in Figure 1. It will work at luminosity $10^{34}\ cm^{-2}s^{-1}$. Proton beams will collide there every 25 ns during which come to 23 interactions.

There are several regions of physics where ATLAS can significantly contribute. Those are [6]:

- Higgs boson searches. For measurement in full range of possible Higgs boson masses is essential high resolution for electrons, muons, photons, jets and E_T^{miss} and also excellent secondary vertex detection for τ-leptons and b-quarks.
- SUSY. Measurement of E_T^{miss} and b-tagging is important.
- new heavy gauge bosons. This measurement requires high resolution for leptons in the range of several TeV in p_T
- quark compositeness. It needs measurement of high-p_T jets.
- precision measurement of W boson and top quark masses, gauge bosons coupling, measurement of the properties of weak bosons, CP violation and the determination of the Cabibbo-Kobayashi-Maskawa unitarity triangle. This needs precise control of the energy scale for jets and leptons, precise determination of secondary vertices, full reconstruction of final states with relatively low-p_T particles and trigger on low-p_T leptons.

The E-p scale uncertainty is one of sources of systematical errors. Its influence over the Z boson mass, p_T and rapidity distributions needs to be investigated. Fully simulated data sample is used for this investigation. This influence can be deduced from changes of some parameters (mean value, FWHM and χ^2/NDF) of these distributions. Kolmogorov-Smirnov test of goodness of fit is another useful tool. It is statistical test investigating whether two one-dimensional sets of points are compatible with coming from the same parent distribution. It allows to see how much distribution with non-zero uncertainty of the E-p scale differs from distribution with uncertainty of the E-p scale 0.00 %.

This project consists of two parts. Part one is dedicated to description of the experiment ATLAS. It deals with its overall functioning, function of its parts and some of their properties. Determination of E-p scale and electron and photon reconstruction and identification in the ATLAS detector are also briefly mentioned. Part two shows a results of investigation of influence of uncertainty of E-p scale on mass, momentum and rapidity of Z boson.

Chapter 2

LHC accelerator

LHC (Large Hadron Collider) accelerator (Figure 2.2) in CERN (Conseil Européen pour la Recheche Nucléaire - European Organization for Nuclear Research) is primarily designed for collisions of two proton beams with energy of 14 TeV in the centre of mass. It is built in existing LEP (The Large Electron-Positron Collider) tunnel. The LHC project was approved by CERN Council in December 1994.

There are four large experiments placed on LHC - ALICE (A Large Ion Collider Experiment), ATLAS (A Toroidal LHC ApparatuS), CMS (Compact Muon Solenoid) and LHCb (The Large Hadron Collider beauty experiment).

ATLAS and CMS are general-purpose detectors. Their basic task is to elucidate electroweak symmetry breaking and to search for Higgs boson. There is also possibility of discovery of particles predicted by Supersymmetry (SUSY).

LHCb is conceived to study CP violation and other rare phenomena in B meson decays. Study of B meson decays will be possible also for ATLAS and CMS.

ALICE is general-purpose heavy-ion detector. It is designed to study physics of strongly-interacting matter and the quark-gluon plasma. Study of ion-ion collisions will be also possible for ATLAS and CMS.

Aside of proton-proton collisions, there are also planned ion-ion collisions with ions $^{208}Pb^{82+}$ and beam energy 2.76 TeV/nucleon. For more details see Table 2.1.

General information		
Ring circumference [m]	26658.883	
Number of collision points	4	
	p-p collisions	Pb-Pb collisions
Energy in the centre of mass	14 TeV	2.76 TeV/nukleon
Luminosity $[cm^{-2}s^{-1}]$	10^{34}	1.0×10^{27}
Numbers of particles/ions per bunch	1.15×10^{11}	7×10^{7}
Number of bunches	2808	592
Time between collisions [ns]	24.95	99.8
Total cross section [mb]	100	514000
Beam current lifetime [hour]	44.86	21.8

Table 2.1: Some properties of LHC accelerator

Protons get into LHC through LHC injector chain (Figure 2.1), which consists of linear accelerator Linac2 (where they gain energy 50 MeV) and synchrotrons PSB (Proton Synchrotron Booster - 1.4 GeV), PS (Proton Synchrotron - 25 GeV) a SPS (Super Proton Synchrotron - 450 GeV). From SPS are protons injected into LHC.

For heavy ions it is different because PSB cannot achieve required density. Thus, heavy ions start in linear accelerator Linac3 (where they gain energy 4.2 MeV/nucleon) and continue through LEIR (Low Energy Ion Ring - 72.2 MeV/nucleon), PS (5.9 GeV/nukleon), SPS (176.4 GeV/nukleon) and ends in LHC ([3] a [4]).

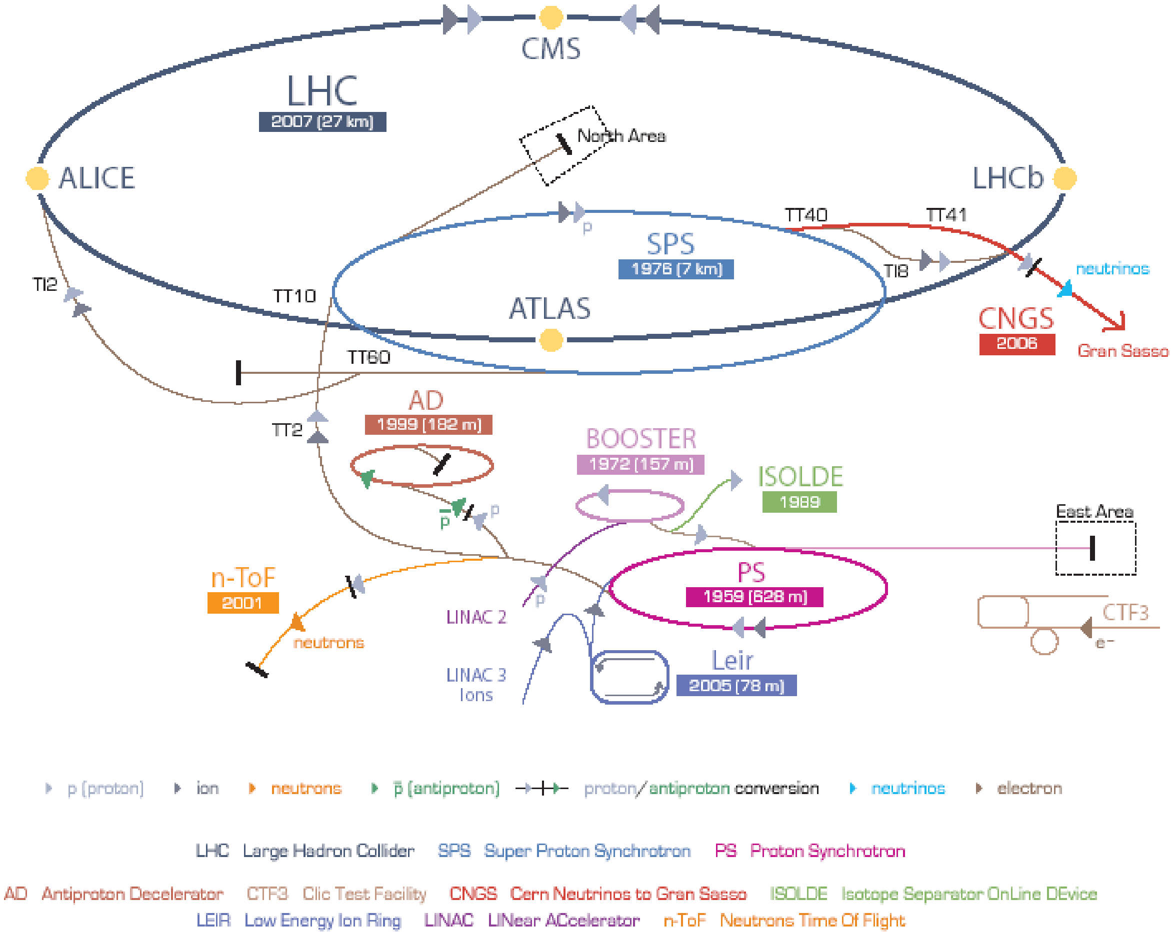

Figure 2.1: LHC injector chain

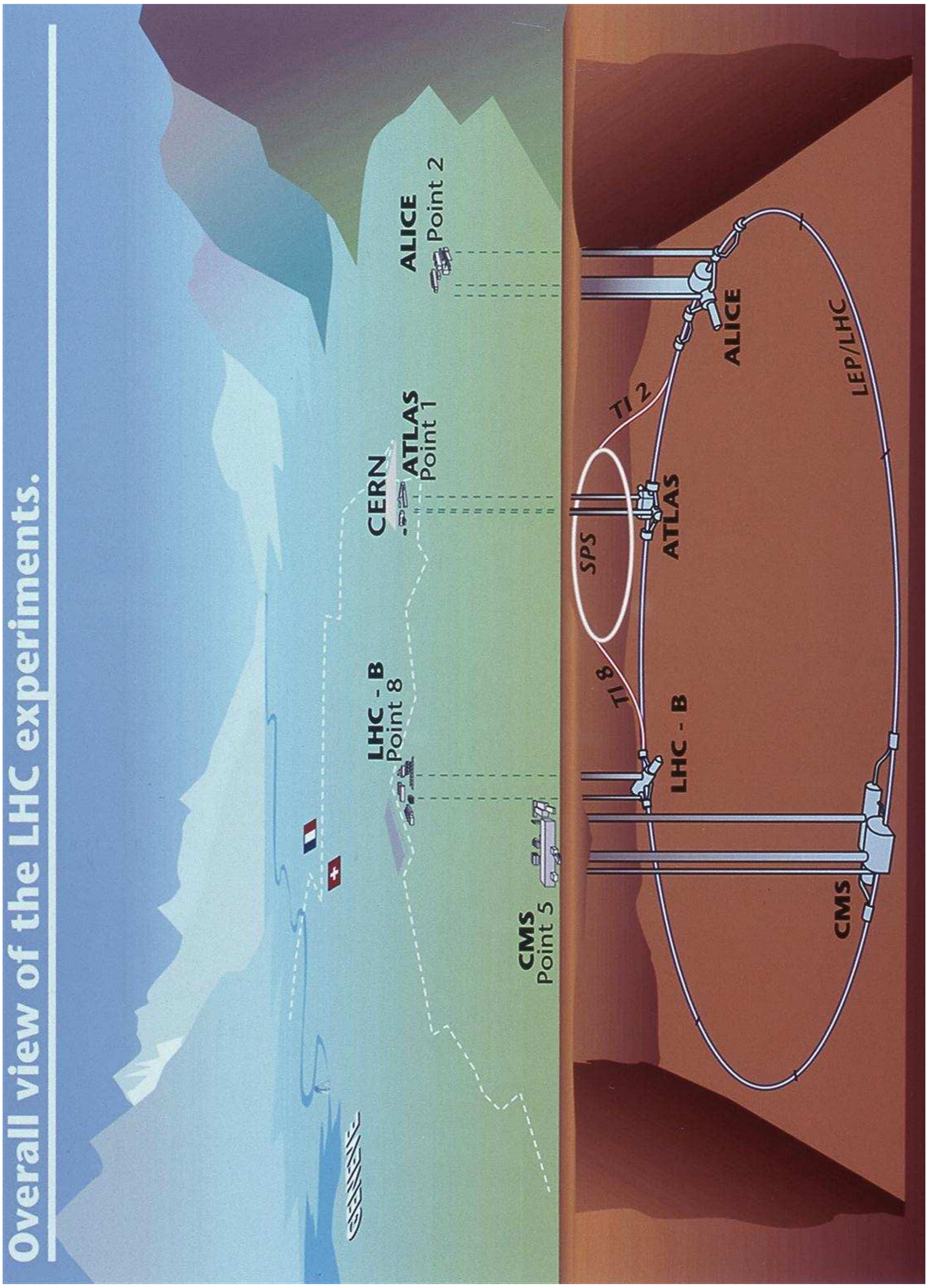

Figure 2.2: LHC accelerator and experiments located there

Chapter 3

Detector

3.1 Nomenclature

3.1.1 Coordinate system

Cartesian coordinate system

Here are shown definitions of coordinate systems in ATLAS detector. The z-axis is defined by beam direction. The x-y plane is transverse to beam direction. The positive x-axis is pointing from the interaction point to the centre of LHC ring. Positive y-axis is pointing upwards. The side A of the detector is defined as the side with $z > 0$. The side C is the side with $z < 0$. Side B is the plane with $z = 0$.

Spherical coordinate system

Spherical coordinate system is established in standard way (Figure 3.1).

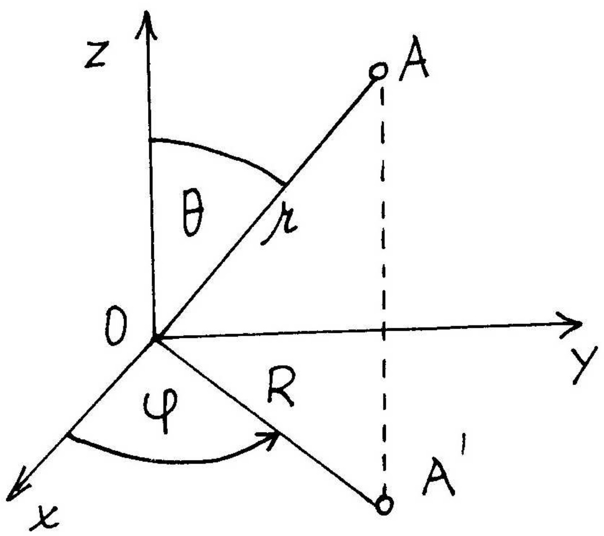

Figure 3.1: Spherical coordinate system

Other important physical quantities

- pseudorapidity (Figures 3.2 and 3.3), defined as $\eta = -\ln\tan(\frac{\theta}{2})$

- transverse momentum p_T
- transverse energy $E_T = E \sin\theta$
- missing transverse energy $E_T^{miss} = E^{miss} \sin\theta$
- distance as a function of pseudorapidity and azimuthal angle $\Delta R = \sqrt{\Delta^2\eta + \Delta^2\phi}$

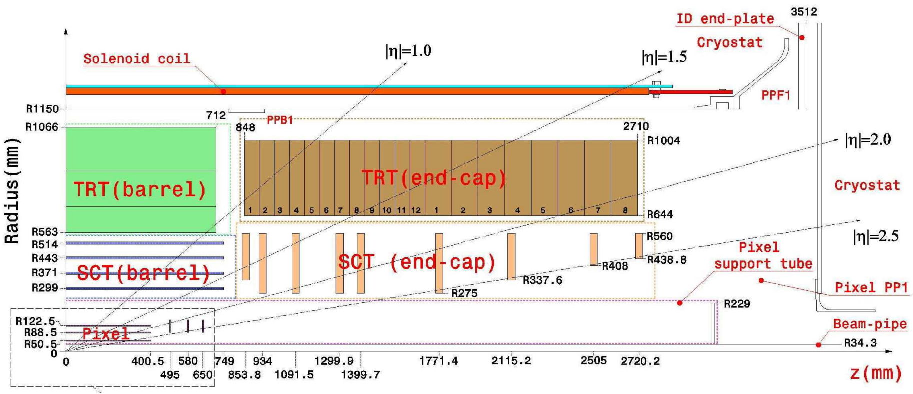

Figure 3.2: Plain view of a quarter-section of the ATLAS inner detector. Lines show some values of pseudorapidity.

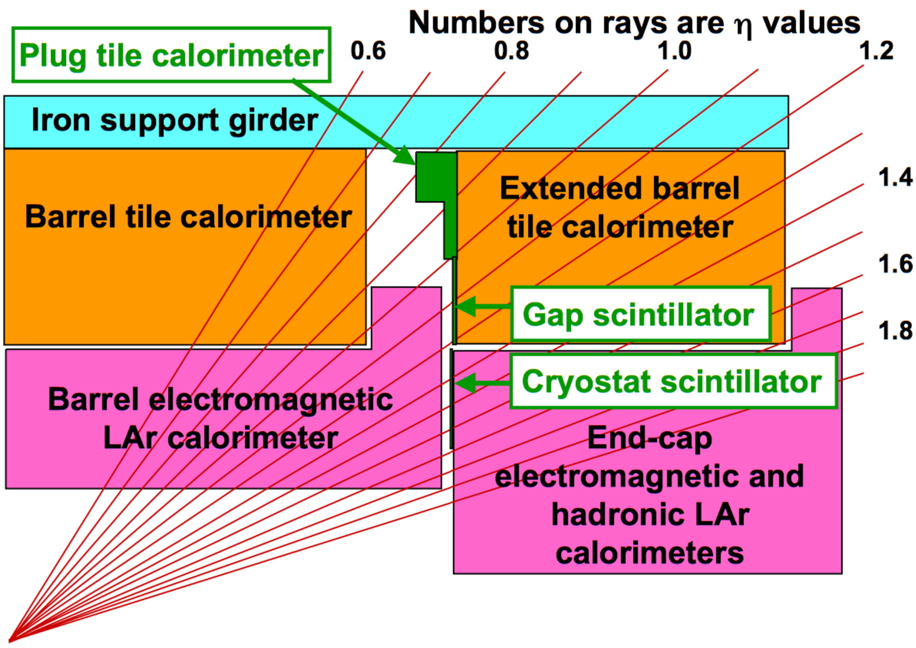

Figure 3.3: Plain view of a quarter-section of the ATLAS calorimeters. Lines show some values of pseudorapidity.

3.1.2 Parameters describing particles in magnetic field

There are five helix parameters which describe trajectories of charged particles in an ideal uniform magnetic field. This parametrization is used in ATLAS.
Parameters defined in x-y plane:

- reciprocal of the transverse momentum with respect to the beam axis

$$\frac{\mathbf{1}}{\mathbf{p_T}}$$

- azimuthal angle ϕ

$$\tan\phi \equiv \frac{p_y}{p_x}$$

- transverse impact parameter $\mathbf{d_0}$, defined as the transverse distance to the beam axis at the point of closest approach

Parameters defined in R-z plane:

- cotangent of the polar angle

$$\cot\theta \equiv \frac{p_z}{p_T}$$

- longitudinal impact parameter $\mathbf{z_0}$, defined as z position of the track at the point of closest approach

3.2 Inner detector

The Inner Detector (ID) (Figures 3.4, 3.5 and 3.6) is detector system closest to the interaction point. It is immersed in a 2 T magnetic field generated by the central solenoid. ID consists of a barrel and two end-caps. It is used for pattern recognition, primary and secondary vertex measurement, electron identification.

The precision tracking detectors (pixels and semiconductor tracker (SCT)) are arranged on concentric cylinders around the beam axis (in the barrel) or on discs perpendicular to the beam axis (in the end-caps). They cover the region $|\eta| < 2.5$. Each track crosses three pixel layers and eight strip layers. The silicon sensors must be kept at low temperature (~ -5 to $-10°C$).

The last detector in the ID is the transition radiation tracker (TRT). It is made of straw (tube) detectors. They are parallel to the beam axis (in the barrel) or arranged radially on wheels (in the end-caps). There are typically 36 hits per track. The TRT is designated to operate at room temperature.

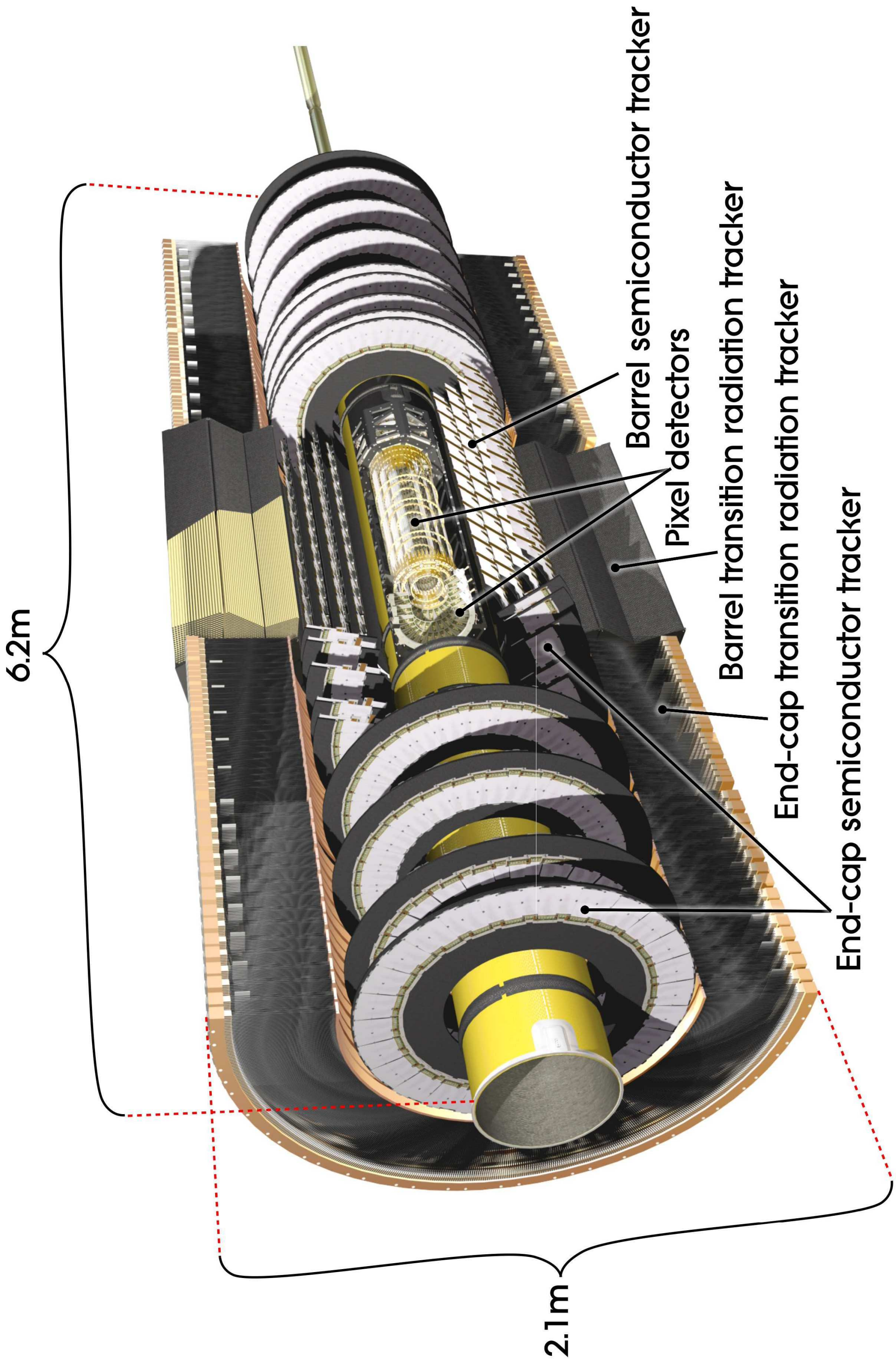

Figure 3.4: The ATLAS inner detector

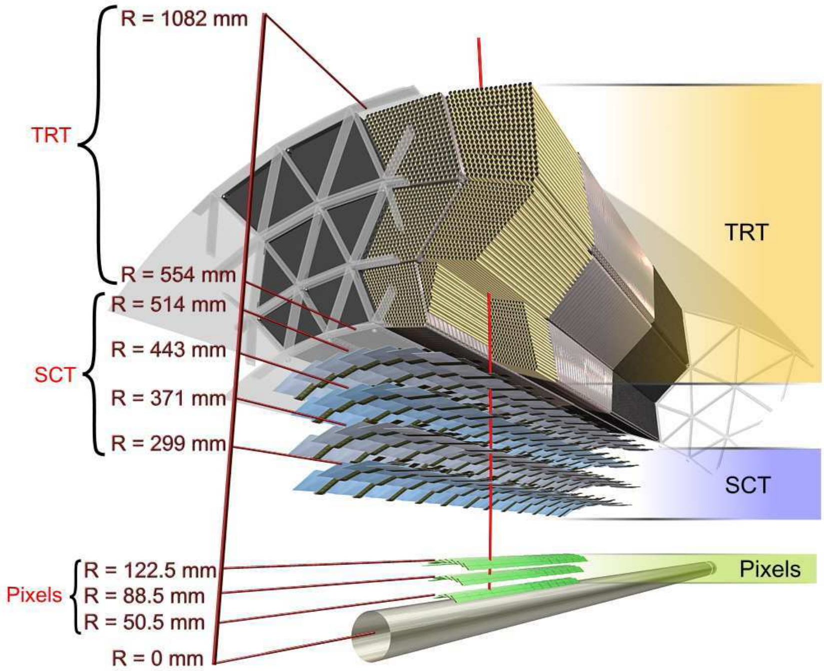

Figure 3.5: Drawing showing the sensors and structural elements of the ID

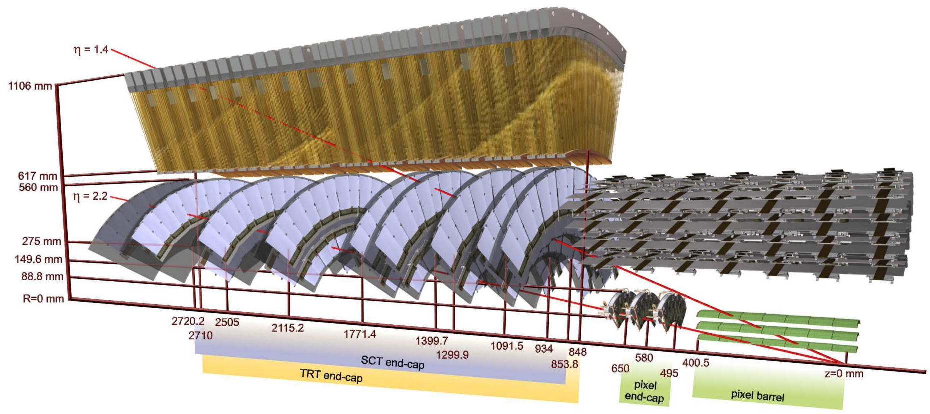

Figure 3.6: Drawing showing the sensors and structural elements of the ID

3.2.1 Pixels

The pixel detector (Figure 3.7) consists of 1744 identical sensors. The pixel sensors are arranged in three layers in the barrel and three disks in the end-cap. The minimum pixel size is 50×400 μm. There are 47232 pixels on each sensor. From each sensor go 46080 readout channels. The pixel detector has approximately 80.4 million readout channels. The main parameters of the pixel detector are summarised in Table 3.1.

Item		Radial extension (mm)	Length (mm)
Pixel	Overall envelope	45.5<R<242	0<|z|<3092
3 cylindrical layers	Sensitive barrel	50.4<R<122.5	0<|z|<400.5
2×3 discs	Sensitive end-cap	88.8<R<149.6	495<|z|<650

Table 3.1: Main parameters of the pixel detector

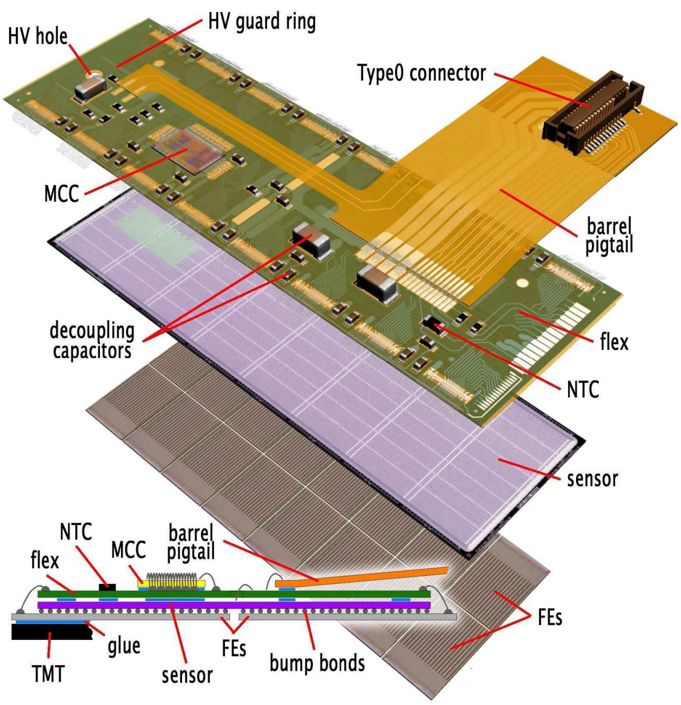

Figure 3.7: Schematic view of a barrel pixel module

3.2.2 SCT

The SemiConductor Tracker (Figure 3.8) consists of 4088 modules. They are arranged in four coaxial cylindrical layers (in the barrel) and nine disk layers (in the end-caps). The barrel module consists of four sensors, two each on the top and bottom side. Each of end-caps modules has two sets of sensors glued back-to-back. There are 1536 sensor strips per module. The sensor thickness is 285 ± 15 μm and the strip pitch is $\sim 80 \mu m$. There are 768 active strips per sensor. The total number of readout channels is approximately 6.3 million. The main parameters of the SCT are summarised in Table 3.2.

Item		Radial extension (mm)	Length (mm)
SCT	Overall envelope	255<R<549 (barrel)	0<|z|<805
		251<R<610 (end-cap)	810<|z|<2797
4 cylindrical layers	Sensitive barrel	299<R<514	0<|z|<749
2 × 9 discs	Sensitive end-cap	275<R<560	839<|z|<2735

Table 3.2: Main parameters of the SCT

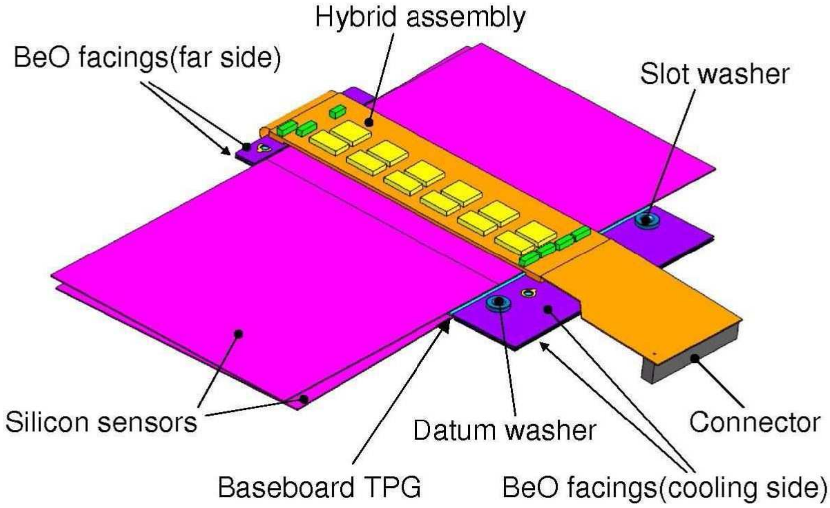

Figure 3.8: Drawing of a barrel module

3.2.3 TRT

The basic detector element of the Transition Radiation Tracker (Figure 3.9) is polyimide drift tube (straw tube). It has diameter of 4 mm. The straw tube wall is 35 μm thick. The straw anode is tungsten wire of 31 μm diameter. There are up to 73 layers of straws interleaved with fibres (in the barrel) and 160 straw planes interleaved with foils (in the end-caps). The TRT in the barrel is divided into three rings with 32 modules each. The TRT in the end-caps consists of two sets of independent wheels. The set closer to the interaction point contains 12 wheels. The outer set contains 8 wheels. Each layer contains 768 radially oriented straws. The total number of TRT readout channels is approximately 351000. The main parameters of the TRT are summarised in Table 3.3.

The TRT detects electrons either passing through the detector or created in interaction of photon with Xe-based gas mixture (consisting of Xe, CO_2 and O_2) inside of the tube. Low-energy transition radiation photons are absorbed in the Xe-based gas mixture.

Item		Radial extension (mm)	Length (mm)
TRT	Overall envelope	554<R<1082 (barrel)	0<|z|<780
		617<R<1106 (end-cap)	827<|z|<2744
73 straw planes	Sensitive barrel	563<R<1066	0<|z|<712
160 straw planes	Sensitive end-cap	644<R<1004	848<|z|<2710

Table 3.3: Main parameters of the TRT

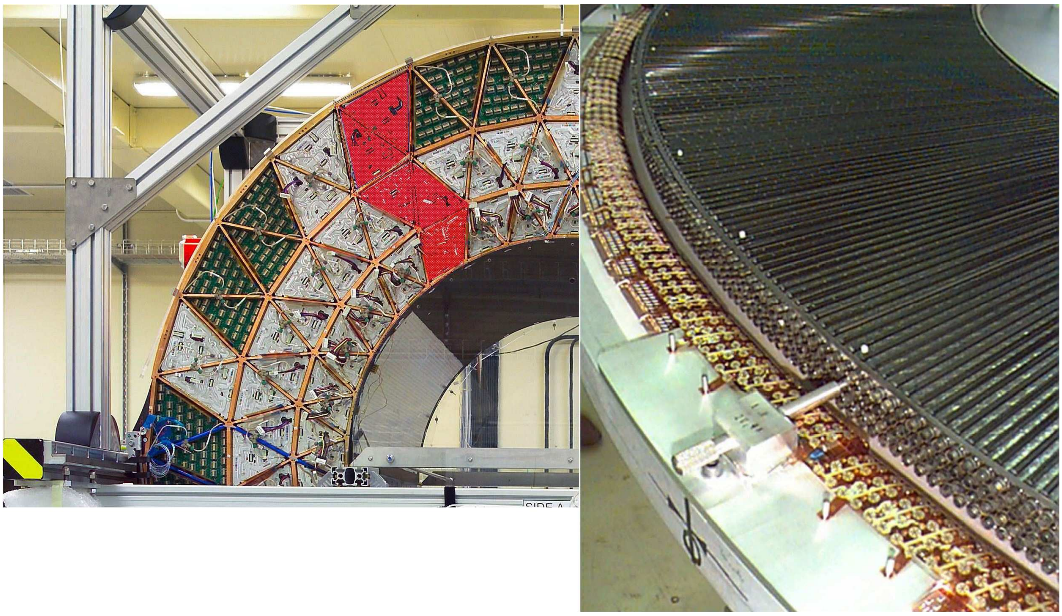

Figure 3.9: On the left is a photograph of one quarter of barrel TRT. On the right is a photograph of a four-plane TRT end-cap wheel.

3.3 Calorimetry

Calorimetry is based on phenomena, when some types of particles with high energy cause secondary particles showers (passing through the material of suitable properties). The shower is caused by inelastic interaction with absorber material. Secondary particles have also ability to create showers. Thus, the avalanche arises. This process ends, when energy of particles decreases under some limit. That means the whole energy of the incomming particle is absorbed in the material. Fraction of this energy is transformed into measurable signal. Fluctuations of magnitude of this fraction define detector resolution.

Calorimeters elicit energy from absorption of charged or neutral particles. They are able to find a type, energy and position of particle.

Calorimeters system of the ATLAS detector (Figure 3.10) has full ϕ-symmetry and covers the range $|\eta| < 4.9$. It consists of the Electromagnetic Calorimeter (EM), the Hadronic End-cap calorimeter (HEC), the Forward Calorimeter (FCal) (all of these use liquid argon as active detector medium for its intrinsic linear behavior, stability of response over time and its intrinsic radiation-hardness) and the Tile calorimeter (which using scintillating tiles).

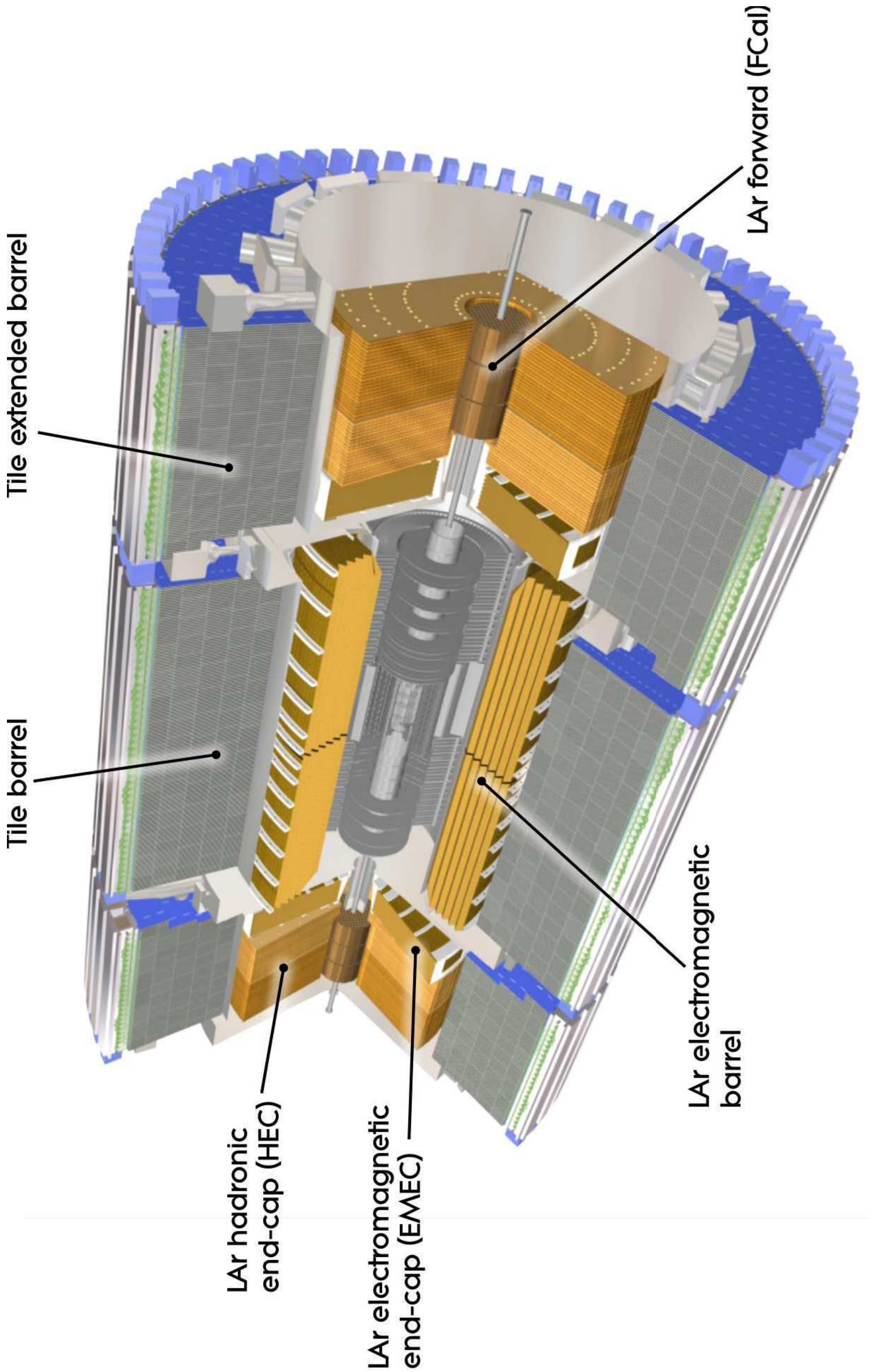

Figure 3.10: The ATLAS calorimeter system

3.3.1 Description of showers

Electromagnetic showers

Electromagnetic showers can arise, when high-energy electron (positron) or γ flies in sufficiently deep block of material and interact with matter. Shower is controlled by electromagnetic interaction

Processes, important for electron (positron) interactions are:

- collisions with atoms (ionization, excitation of atoms)
- bremsstrahlung
- positrons can annihilate

Processes, important for photon interactions are:

- photoelectric effect (ionization, excitation of atoms)
- Compton scattering (ionization, excitation of atoms)
- pair production

Dominant process for electrons (positrons) with energy over 1 GeV is bremsstrahlung. For photons it is pair production.

In connection with the electromagnetic showers, the term radiation length X_0 needs to be introduced. It is mean value of the distance, when high-energy electron will have only fraction $\frac{1}{e}$ of its original energy E_0. Energy losses are caused by bremsstrahlung the particle produce in material on a path of length x and holds

$$< E >= E_0 \exp(-\frac{x}{X_0})$$

For high-energy photons ($\gamma \longrightarrow e^+e^-$) holds:

$$I_\gamma = I_0 \exp(-\frac{7x}{9X_0})$$

where I is radiation intensity. X_0 is used as unit for longitudinal dimension of the shower.

Hadronic showers

Hadronic showers are cascades of the deep inelastic interactions of incomming hadrons with nuclei. Shower is controlled by strong interaction.

High-energy hadron interaction with nucleus has two phases:

- quick - multiparticle production
- slow - fission and deexcitation of nucleus

First phase: About half of energy is used to create new particles and to knock out nucleons from the nucleus. Another half is carried by incomming particle or bunch of particles with same quantum numbers (leading particle effect).

Second phase: The nucleus can fission after interaction. There are created excited daughter nuclei. They dispose energy by evaporating nucleons (mostly neutrons) and by emitting photons.

In connection with the hadronic showers, the term absorption length λ_0 needs to be introduced. It is a mean free path between two inelastic nuclear interactions and holds

$$\lambda_0 = \frac{A}{N_{AV}\rho\sigma_i}$$

where A is atomic number, N_{AV} is Avogadro's number, ρ is density and σ_i is inelastic cross section. λ_0 is used as unit for longitudinal dimension of the shower.

3.3.2 Electromagnetic calorimetry

The electromagnetic calorimeter is sensitive to electrons (positrons) and photons. It is divided into a barrel part (Figure 3.12) and two end-caps (Figure 3.13). The barrel calorimeter consists of two identical half-barrels (centered around the z-axis), separated by a small gap. Each end-cap calorimeter is divided into two coaxial wheels (see Table 3.4 for main parameters of the electromagnetic calorimeter).

	Barrel		End-cap	
Number of layers and $\|\eta\|$ coverage				
Presampler	1	$\|\eta\| < 1.52$	1	$1.5 < \|\eta\| < 1.8$
Calorimeter	3	$\|\eta\| < 1.35$	2	$1.375 < \|\eta\| < 1.5$
	2	$1.35 < \|\eta\| < 1.475$	3	$1.5 < \|\eta\| < 2.5$
			2	$2.5 < \|\eta\| < 3.2$
Number of readout channels				
Presampler	7808		1536 (both sides)	
Calorimeter	101760		62208 (both sides)	

Table 3.4: Main parameters of the electromagnetic calorimeter

The electromagnetic calorimeter is detector with accordion-shaped kapton electrodes. It use lead as absorber and liquid argon (LAr) as active medium (Figure 3.11). The accordion geometry provides complete ϕ symmetry without any cracks. In the barrel, the accordion waves are axial and run in ϕ. The half-barrel is made of 1024 accordion-shaped absorbers and is divided into 16 modules (the total thickness of a module is at least 22 radiation lengths). In the end-caps, the waves run axially. Each end-cap contains 768 absorbers in the outer wheel and 256 absorbers in the inner wheel. The end-cap is divided into eight modules (the total thickness of the end-cap calorimeter is greater than 24 X_0 except $|\eta| < 1.475$). The readout electrode consists of three separated conductive copper layers. The electrode is positioned in the middle of the gap of size 2.1 mm. Each barrel gap between two absorbers is equipped with two electrodes. Each end-cap gap between two absorbers is equipped with one electrode.

There is a presampler detector closer to the interaction point than the electromagnetic calorimeter. It is used to correct the energy lost by electrons and photons upstream of the calorimeter. Presampler is separate thin liquid argon layer. It is made of 32 azimuthal sectors per half-barrel (or end-cap).

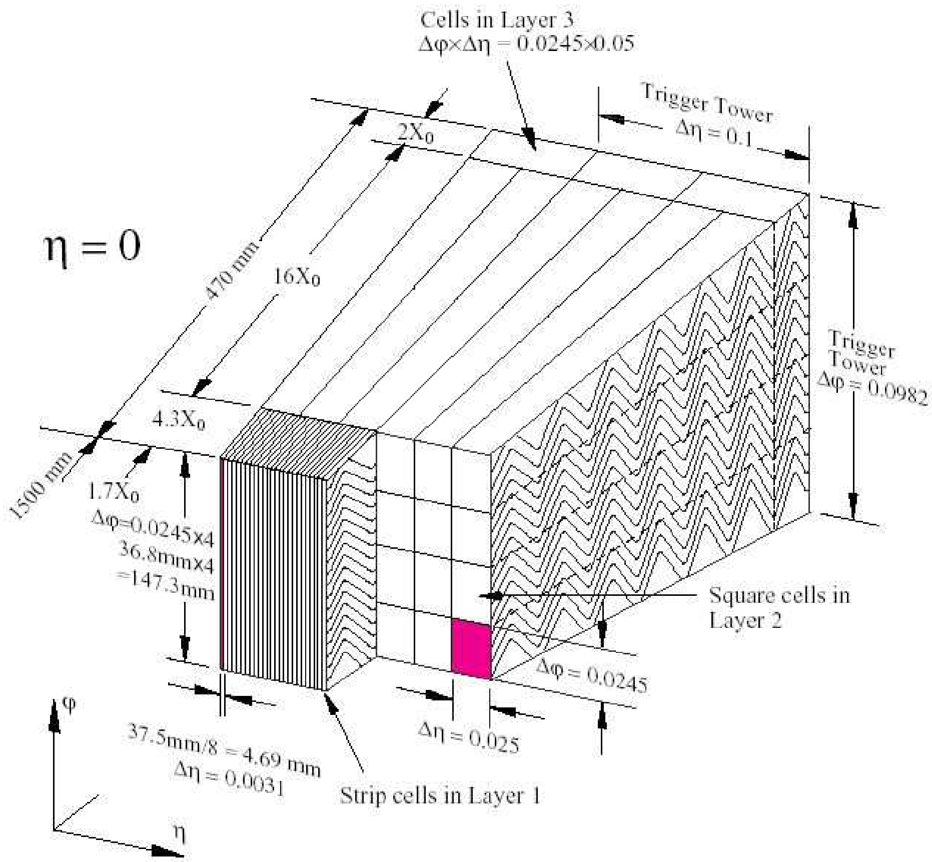

Figure 3.11: Sketch of a barrel module

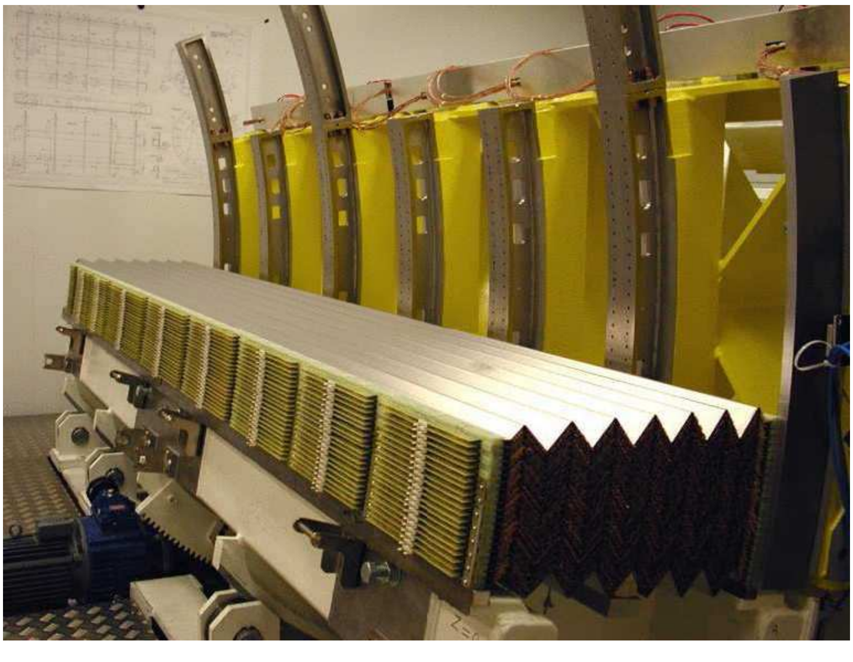

Figure 3.12: Photograph of a partly stacked barrel electromagnetic LAr module.

Figure 3.13: Photograph showing a side view of an electromagnetic end-cap LAr module

3.3.3 Hadronic calorimetry

Tile calorimeter

The tile calorimeter (Figure 3.14) is placed directly outside of the electromagnetic calorimeter. It consists of a barrel part and two extended barrels. Both are divided azimuthally into 64 modules. The radial depth of the tile calorimeter is approximately 7.2 λ. The tile calorimeter is using iron as the absorber and scintillating tiles as the active material. The tiles are 3 mm thick and the total thickness of the iron plates in one period is 14 mm. Two sides of scintillating tiles are read out by wavelength shifting fibres into two separate photomultiplier tubes (PMT) (Figure 3.14). The tile calorimeter is longitudinally segmented into three layers (see Table 3.5 for main parameters of the tile calorimeter).

	Barrel	**Extended barrel**
$\vert\eta\vert$ coverage	$\vert\eta\vert < 1.0$	$0.8 < \vert\eta\vert < 1.7$
Number of layers	3	3
Number of readout channels	5760	4092 (both sides)

Table 3.5: Main parameters of the tile calorimeter

There are eleven sizes of scintillating tiles 3 mm thick, one for each depth in radius. Base material of tiles is polystyrene, creating ultraviolet scintillation light after ionising particle crossing. This light is converted to visible light by wavelength-shifting fluor (the polystyrene is doped with 1.5 % PTP and 0.04 % POPOP). Wavelength-shifting fibres collect (at the edges of each tile) the scintillation light and convert it to a longer wavelength and transmit it to the PMT.

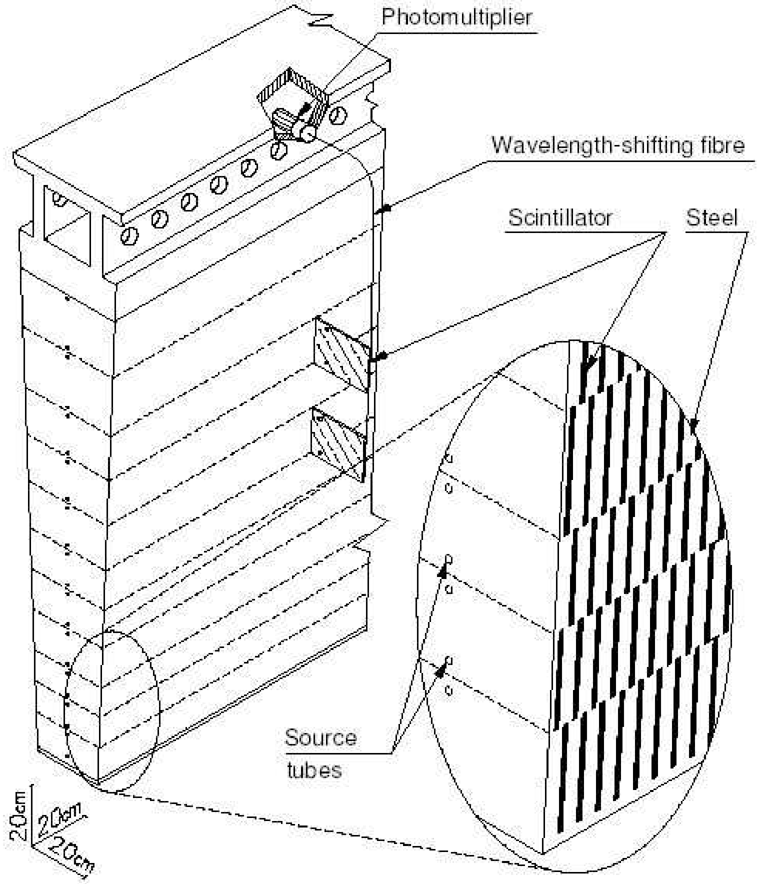

Figure 3.14: Schematic of the tile calorimeter structure geometry

Hadronic end-cap calorimeters (HEC)

The Hadronic End-cap calorimeter consists of two wheel on each end-cap. It uses copper as absorber and liquid argon as an active medium. It is located directly behind the electromagnetic end-cap calorimeters. Each wheel is built from 32 identical modules (Figure 3.15) and is divided into two longitudinal segments. It is a total of four layers per end-cap. The wheels closer to the interaction point are made from 25 mm parallel copper plates. The others use 50 mm copper plates. The copper plates are interleaved with 8.5 mm LAr gaps (see Table 3.6 for main parameters of the Hadronic End-cap Calorimeter). The gap is divided into four separate drift zones by three electrodes. The middle electrode is used for read-out.

	Barrel	**End-cap**
$\|\eta\|$ coverage		$1.5 < \|\eta\| < 3.2$
Number of layers		4
Number of readout channels		5632 (both sides)

Table 3.6: Main parameters of the hadronic end-cap calorimeter

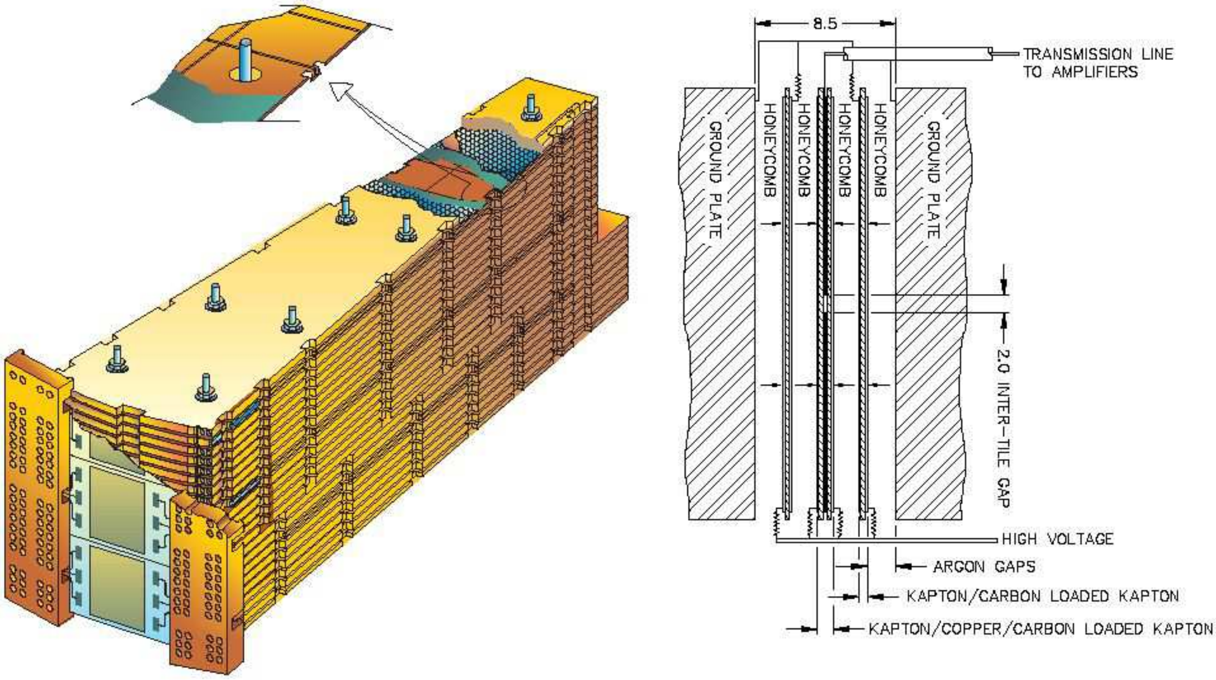

Figure 3.15: Schematic view of the design of a HEC module

Forward calorimeter

The Forward Calorimeter consists of three 45 cm deep modules in each end-cap. First (electromagnetic module) uses copper as absorber and liquid argon as sensitive medium. The other two (hadronic modules) use tungsten as absorber and liquid argon as sensitive medium. Each module consists of metal matrix (Figure 3.16). The matrix is filled with structure consisting of concentric rods and tubes parallel to the beam axis. Between the rod and the tube is the gap filled with liquid argon (see Table 3.7 for main parameters of the Hadronic Forward Calorimeter). Readout electrodes are hard-wired together with small boards on the faces of the modules in groups.

	Barrel	**End-cap**
$\lvert\eta\rvert$ coverage		$3.1 < \lvert\eta\rvert < 4.9$
Number of layers		3
Number of readout channels		3524 (both sides)

Table 3.7: Main parameters of the hadronic forward calorimeter

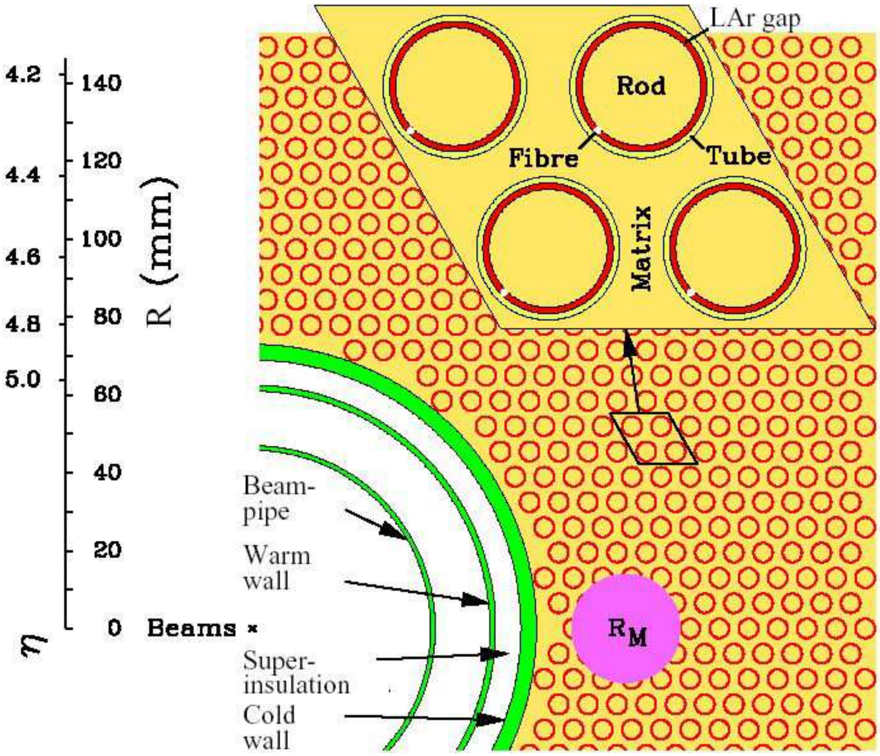

Figure 3.16: Electrode structure of FCal

3.4 Muon spectrometer

High-energy muons are the only charged particles which fly out of the detector volume. The main task of the muon system (Figure 3.17) is to elicit muon tracks and momenta. It is based on the magnetic deflection of muon tracks in the large superconducting air-core toroid magnets.

In the region of $|\eta| < 1.4$ is magnetic bending provided by the large barrel toroid. Over $1.6 < |\eta| < 2.7$ are tracks bent by end-caps magnets. Region $1.4 < |\eta| < 1.6$ is called the transition region and magnetic deflection there is provided by combination of barrel and end-caps fields.

In the barrel region are tracks measured in three cylindrical layers (stations) around the beam axis. In the transition and end-cap regions, there are three stations installed in planes perpendicular to the beam.

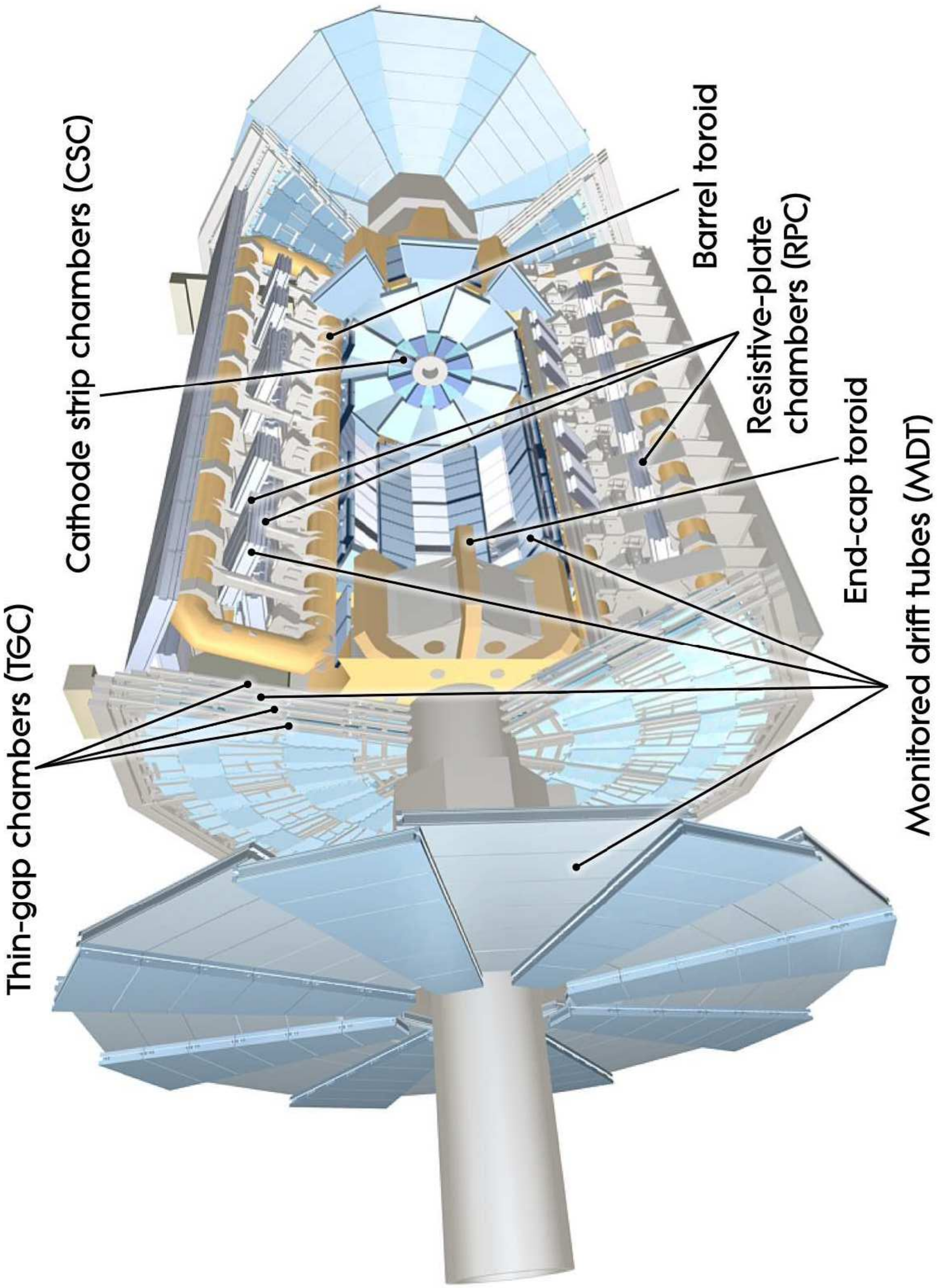

Figure 3.17: The ATLAS muon system

3.4.1 Monitored drift tubes (MDT)

The Monitored Drift Tubes are precision chambers. They consist of drift tubes (Figure 3.18). The drift tube is a tube with diameter of 30 mm filled with mixture of gasses. The electrons from ionisation are collected at the central tungsten-rhenium wire with diameter of 50 μm (see Table 3.8 for main parameters of the MDT's).

The MDT chambers are built of these tubes. The chambers are made in various shapes. They are rectangular in the barrel and trapezoidal in the end-caps. All ordinary chambers consist of two packages of multilayers separated by support structure. Multilayers in the inner layers of muon system consist of four tube layers. In the middle and outer they consist of three tube layers (Figure 3.19).

Gas inside of tube is a mixture of 93 % Ar, 7 % CO_2 and H_2O. It was selected because of the good ageing properties. The disadvantage is non-linear space-drift time. A small water admixture improve HV stability.

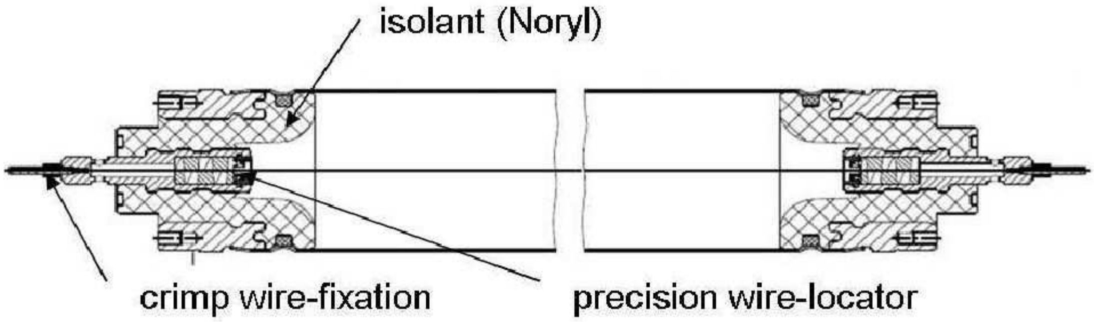

Figure 3.18: Longitudinal cut through a MDT tube

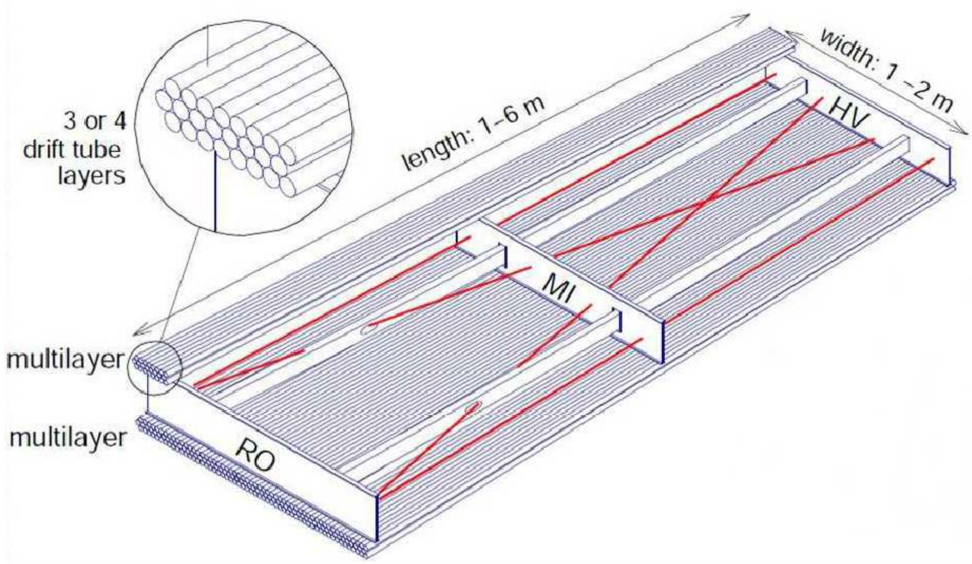

Figure 3.19: Mechanical structure of a MDT chamber

Coverage	$\|\eta\| < 2.7$ (innermost layer $\|\eta\| < 2.0$)
Number of chambers	1108
Number of channels	339000
Function	Precision tracking

Table 3.8: Main parameters of the monitored drift tubes

3.4.2 Cathode strip chambers (CSC)

The Cathode Strip Chambers are precision chambers. In the region where counting rate is too high, some MDT's are replaced by CSC. They have high spatial, time and double track resolution with high-rate capability and low neutron sensitivity. The CSC are segmented into large and small chambers. The whole system consists of two discs. Each disc is segmented into eight chambers (eight small and eight large). Each chamber contain four CSC planes.

The CSC are multiwire proportional chambers (Figures 3.20 and 3.21). Their cathodes are segmented. One has strips perpendicular to wires and the other parallel. Gas inside is a mixture of 80 % Ar and 20 % CO_2 (see Table 3.9 for main parameters of the CSC's).

Coverage	$2.0 < \|\eta\| < 2.7$
Number of chambers	32
Number of channels	31000
Function	Precision tracking

Table 3.9: Main parameters of the cathode strip chambers

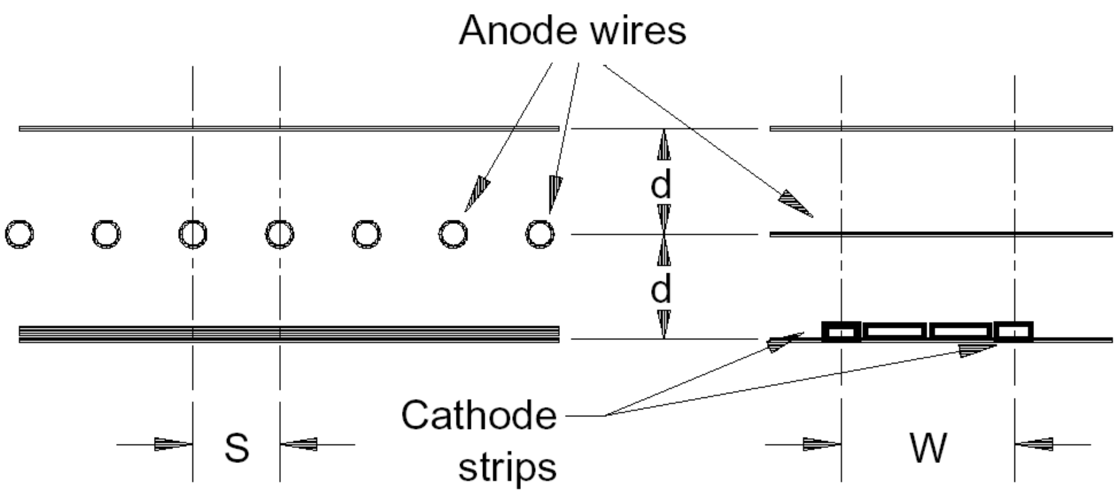

Figure 3.20: Structure of the CSC cell

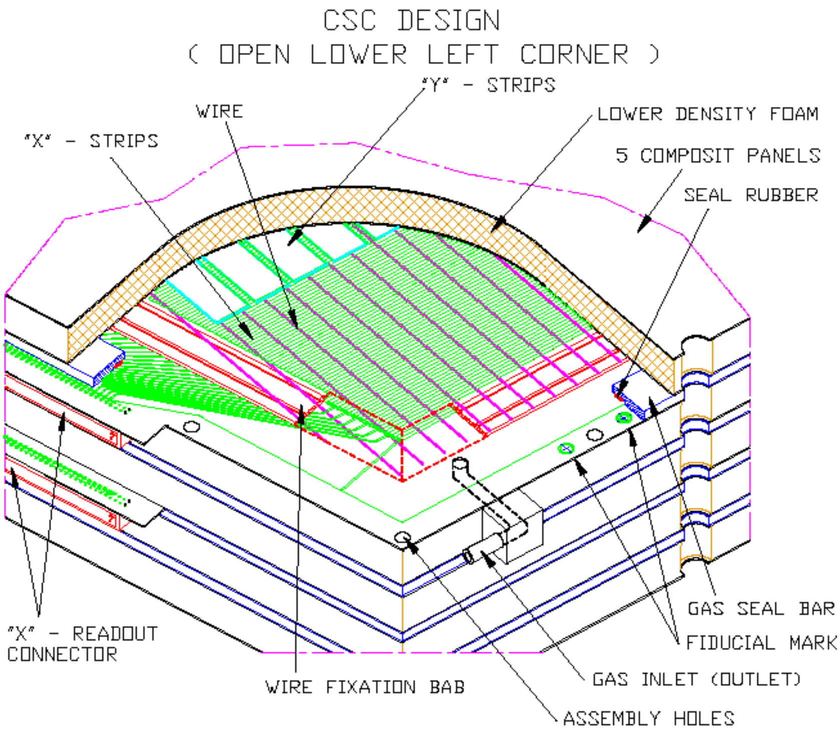

Figure 3.21: Structure of the CSC

3.4.3 Resistive plate chambers (RPC)

The Resistive Plate Chambers are trigger chambers in the barrel region. They are gaseous parallel-plate detectors without wires (Figure 3.22). Two parallel plastic laminate plates are inside of detector. Between them is an electric field. This gap is filled with non-flammable mixture of gasses (mixture of 94.7 % of $C_2H_2F_4$, 5 % of Iso-C_4H_{10} and 0.3 % of SF_6).

The chamber is made of two rectangular detectors (Figure 3.23) called unit. Each unit has two independent resistive plate structures called gas volumes. The structure of the gas volumes are identical for all RPC's. They consist of two resistive plates enclosing gas gap of 2 mm. The outer surface of the resistive plates is coated with thin layer of graphite (see Table 3.10 for main parameters of the RPC's).

Coverage	$\|\eta\| < 1.05$
Number of chambers	544
Number of channels	359000
Function	Triggering, second coordinate

Table 3.10: Main parameters of the resistive plate chambers

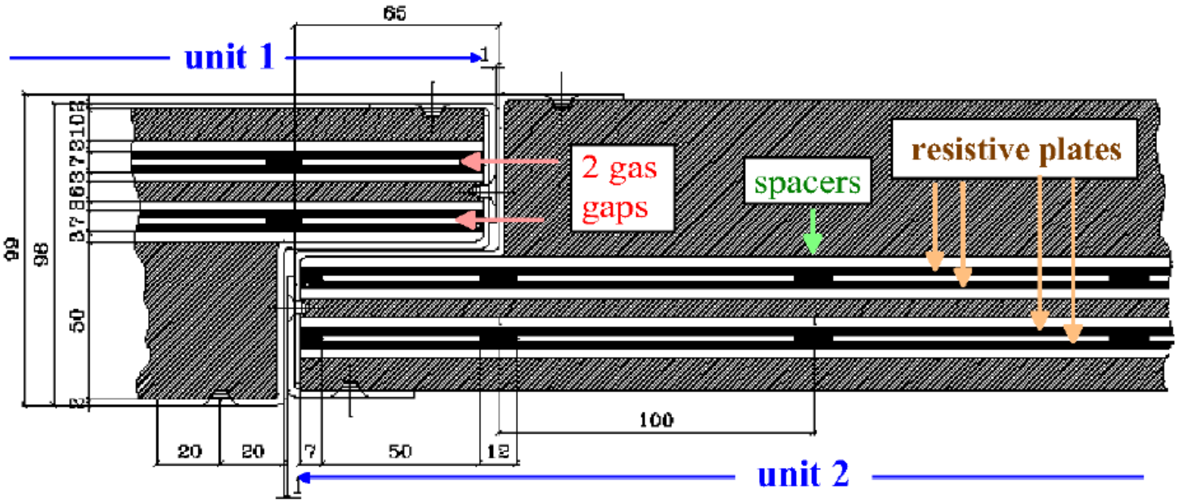

Figure 3.22: Cross section through a RPC, where two units are joined to form a chamber

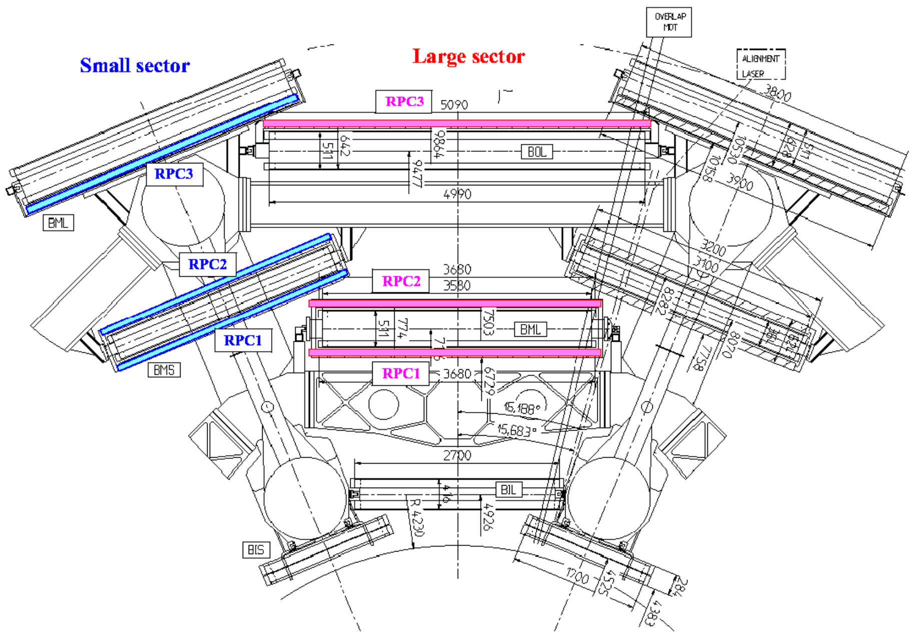

Figure 3.23: Cross section through a upper part of the barrel

3.4.4 Thin gap chambers (TGC)

The Thin Gap Chambers are trigger chambers in the end-caps. They are multiwire proportional chambers with very good resolution. Their wire-to-cathode distance is smaller than the wire-to-wire distance (Figure 3.24). They are filled with gas mixture (55 % of CO_2 and 45 % of n-C_5H_{12}).

The trigger detectors are mounted in two concentric rings (outer covering $1.05 < |\eta| < 1.92$ and inner covering $1.92 < |\eta| < 2.4$). There are seven detector layers arranged in one triplet and two dublets (see Table 3.11 for main parameters of the TGC's).

Coverage	$1.05 < \|\eta\| < 2.4$
Number of chambers	3588
Number of channels	318000
Function	Triggering, second coordinate

Table 3.11: Main parameters of the thin gap chambers

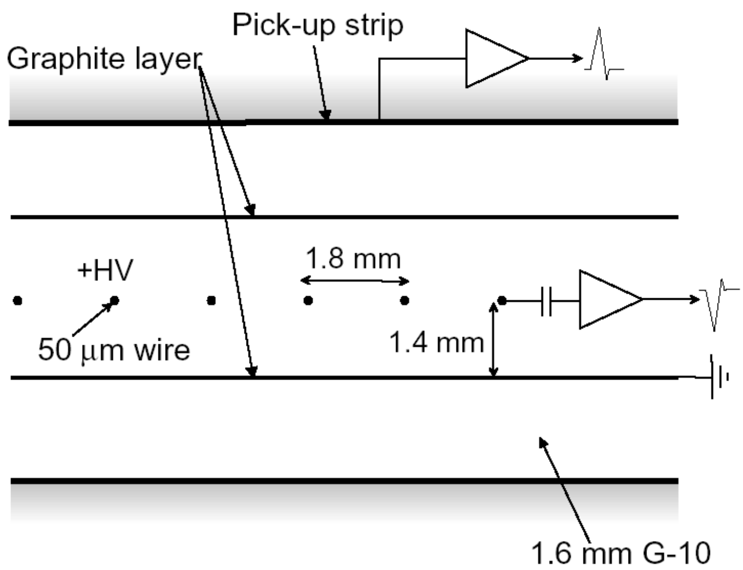

Figure 3.24: TGC structure

3.5 Trigger and data acquisition

The trigger consists of three levels of event selection. It is Level-1 (L1), Level-2 (L2) and Event Filter. The L2 and the Event filter together form the High-Level Trigger (HLT) (see Figure 3.25 for a block diagram).

The L1 trigger searches for high-p_T muons, electrons, photons, jets, τ-lepton decaying into hadrons. It uses reduced-granularity information. Information from RPC and TGC are used for high-p_T muons. Information from calorimeters are used for electromagnetic clusters, jets, τ-lepton, E_T^{miss} and large total transverse energy. The maximum L1 accept rate is 75 kHz (upgradeable to 100 kHz). L1 decision time must be less than 2.5 μs.

The L2 trigger is seeded by Regions-of-Interests (RoI's). RoI's are regions of the detector where the L1 trigger has identified possible trigger objects within the event. The L2 trigger uses RoI information on coordinates, energy and type of signature. It is analysing full-granularity and full-precision data from all detectors. It reduces the event rate below 3.5 kHz. The average processing

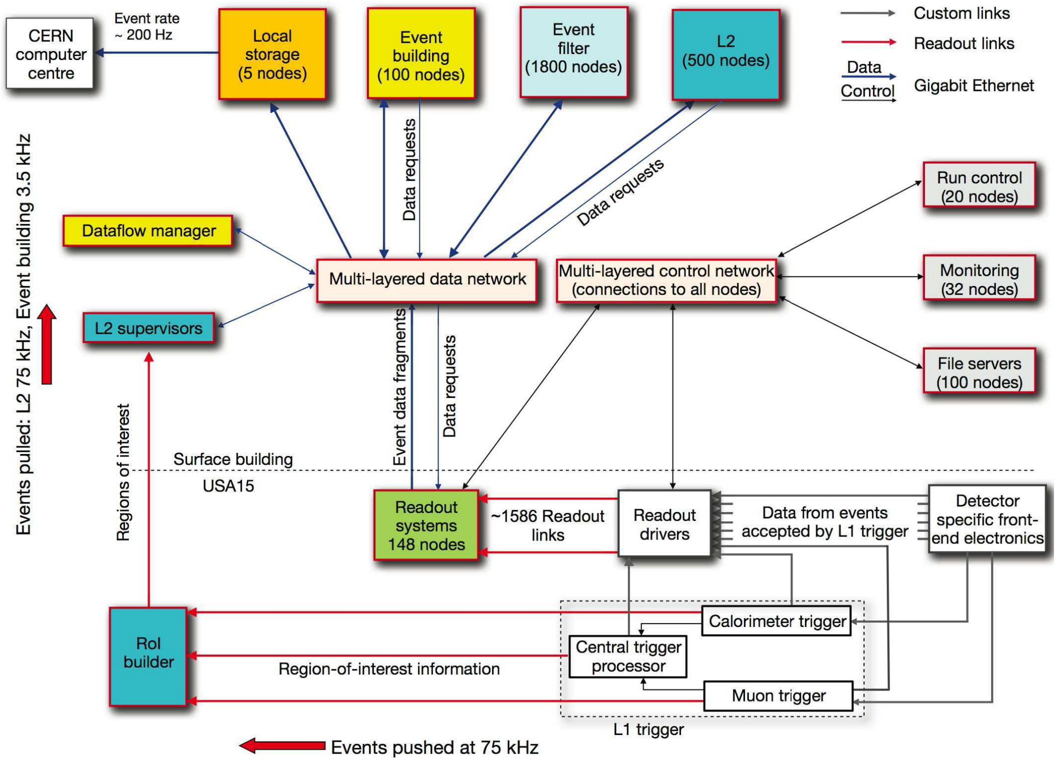

Figure 3.25: Block diagram of the ATLAS trigger and data acquisition system

time is approximately 10 ms.

The event filter uses offline analysis procedure on fully-built events. The event rate is reduced to approximately 200 Hz. The average processing time is of order one second.

The HLT use full-granularity and full-precision of calorimeter and muon chambers (and full data from inner detector).

The data acquisition system (DAQ) receives and buffers the event data from the detector electronics at L1 level. Some of them are moved into L2 trigger and then to the event-building (if they fulfill criteria).

3.5.1 The L1 trigger

The L1 trigger (Figure 3.26) performs the initial event selection. Decisions are based on information from calorimeters and muon system. These decisions are based only on the multiplicity of trigger objects. But information about the geometric location of trigger objects is retained in detector trigger processor. When the event is accepted by the L1 trigger, the information is sent as RoI's to the L2 trigger.

The L1 Calorimeter Trigger (L1Calo) aims to identify high-p_T electrons and photons, jets, τ-lepton decaying into hadron, events with large E_T^{miss} and large total transverse energy. For electron, photon and τ triggers is required isolation, i.e. energetic particle must have a minimum angular separation from any jet in the same candidate trigger.

The L1 muon trigger is based on signals from RPC's (in barrel) and TGC's (in end-caps). It searches for patterns of hits consistent with high-p_T muons. The logic provide six p_T thresholds (three associated with low-p_T trigger and three associated with high-p_T trigger).

The Central Trigger Processor (CTP) combines the information for different object types. It makes decision to accept event or not.

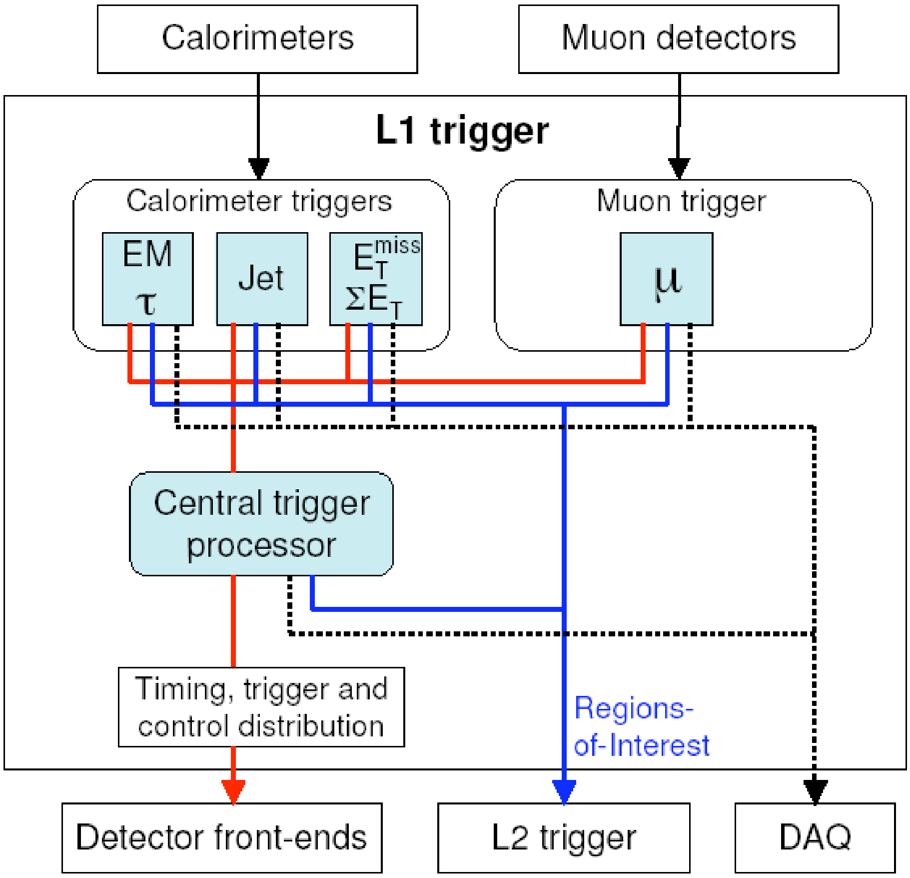

Figure 3.26: Block diagram of the L1 trigger

Calorimeter trigger

L1Calo consists of three main subsystems.

- Pre-processor - it digitises the analogue input signals and uses a digital filter to associate them with specific bunch-crossing. It also does a pedestal subtraction, fine-tune the transverse-energy calibration, ignore small noise pulses and send data to Cluster Processor and Jet/Energy-sum Processor.
- Cluster processor (CP) - It identifies electron/photon and τ-lepton candidates with E_T above the threshold. It is also possible to add certain isolation criteria.
- Jet/Energy-sum Processor (JEP) - It identifies jets and produces global sums of scalar and missing transverse energy

Both CP and JEP count multiplicities of the different types of trigger objects. They send data to the Central Trigger Processor (CTP).

When there is a L1 Accept (L1A) decision from the CTP, the stored data from the L1Calo are read out to the data acquisition system. The types and positions of jets, τ-leptons and electromagnetic clusters candidates are also sent to the RoI builder.

Muon trigger

The L1 muon trigger is based on RPC's in the barrel and the TGC's in the end-caps with three trigger stations each. The algorithm requires coincidence of hits in the different trigger stations within a road, which tracks the path of a muon from the interaction point through the detector. The width of the road is related to the p_T threshold to be applied.

Central trigger processor

The Central Trigger Processor receives trigger information from the calorimeter and muon trigger processor. This information consists of multiplicities for electron/photon, τ-lepton, jets and muons, and of flags indicating which threshold were passed for total and missing transverse energy, and for total jet transverse energy. In the next step the CTP forms trigger conditions (for example, that the multiplicity of a particular muon threshold has exceeded one, i.e. at least two muons in this event have passed this threshold).

3.5.2 High Level Trigger and Data Acquisition

The main components of the HLT/DAQ are: readout, L2 trigger, event-building, event filter, configuration, control and monitoring and information services (Figure 3.25).

After selection by L1 trigger the event data are transferred through the detector specific Readout Drivers (ROD's) to the HLT/DAQ system over Readout Links (ROL's). The event fragments are received into Readout Buffers (ROB's) contained in the Readout System (ROS) unit. They are temporarily stored there.

The L1 trigger also provides the RoI information. The data are transferred through ROL's to the RoI builder. In RoI builder the data are assembled into a single data structure. This structure is forwarded to the L2 supervisor (L2SV). The L2SV receives RoI's, asigns the event to one of the L2 trigger processing units (L2PU's) for analysis, and receives the results.

Requests for event data are made to the associated ROS's (using the RoI information). Results of the analysis are returned to L2SV. L2SV forward it to the DataFlow Manager (DFM). The DMF controls the event during the event-building. If event is selected by the L2 trigger then DMF assigns it to an event-building node (SFI). The SFI collects the event data and builds single event-data structure, the event, which is sent to the event filter for further analysis.

The event filter classifies the selected events. The result of this classification is added to the event structure. Selected event is subsequently sent to the output nodes (SFO's). The events received by the SFO are stored and subsequently transferred to CERN's central data-recording facility.

Control

It covers the control and monitoring of the operational parameters of the detector and experiment infrastructure, the coordination of whole detector, trigger and data acquisition software and hardware associated with data-taking. It consists of two independent parts - the data acquisition control system and Detector Control System (DCS). The data acquisition control system controls the hardware and software elements of the detector and the HLT/DAQ. The DCS controls detector equipment and related infrastructure.

Configuration

Configuration databases maintain description of the hardware and software required for data-taking. A configuration is organized as a tree of linked segments. A segment defines a well defined sub-set of the hardware, software, and their associated parameters.

Monitoring and information distribution

It provides the framework for the routing of operational data and their analysis. The operational data are, for example, physics event data, histograms and the values of parameters, etc. The routing is performed by the information, on-line histogramming and event monitoring services.

Readout system

The ROS receives event data from the detector ROD's via ROL's. The ROL has homogenous design and implementation. ROB's are buffers located at receiving end of the ROL's. A L2PU request for data involves one or two ROB's per ROS on average. The event-building nodes request the event data from all the ROB's of a ROS.

L2 trigger

The L2 trigger combines functions of RoI builder, L2SV, L2PU and L2 trigger-specific ROS. The RoI builder receives the RoI information from L1 trigger and merges it into a single data structure and transfers it into L2SV. The L2SV marshals the event through the L2 trigger. The principal component of the L2 trigger is the L2 processing farm.

Event-building

The event is built by DMF, ROS's and SFI's. The SFI collects data from the ROS's and creates single data structure. The DFM allocates events to the SFI's.

Event filter

The event filter is a processing farm. There runs standard ATLAS event reconstruction and analysis application. For event passing the selection criteria is added a tag to the event data structure identifying into which physics stream (electrons, muons, jets, photons, E_T^{miss}, τ-leptons, B-physics) the event has been classified.

Event output

SFO's receive events from the event filter. They interface HLT/DAQ to CERN's central data-recording facility. The SFO maintains a set of files into which it records event. Each event is recorded in one or more files according to the stream classification.

3.6 Other devices

3.6.1 Magnets

Magnetic field in ATLAS detector is created by hybrid system of four superconducting magnets - one solenoid, one barrel toroid and two end-caps toroids. Magnets are cooled by liquid helium to 4.5 K. It is shown on Figures 1 and 3.27. Some of its parameters are shown in Table 3.12.

The magnet system consists of

- solenoid
- three toroids - one barrel toroid and two end-caps toroids

	Solenoid	Barrel toroid	End-cap toroid
Inner diameter [m]	2.46	9.4	1.65
Outer diameter [m]	2.56	20.1	10.7
Axial length [m]	5.8	25.3	5.0
Peak field in the windings [T]	2.6	3.9	4.1

Table 3.12: Some parameters of ATLAS magnet system

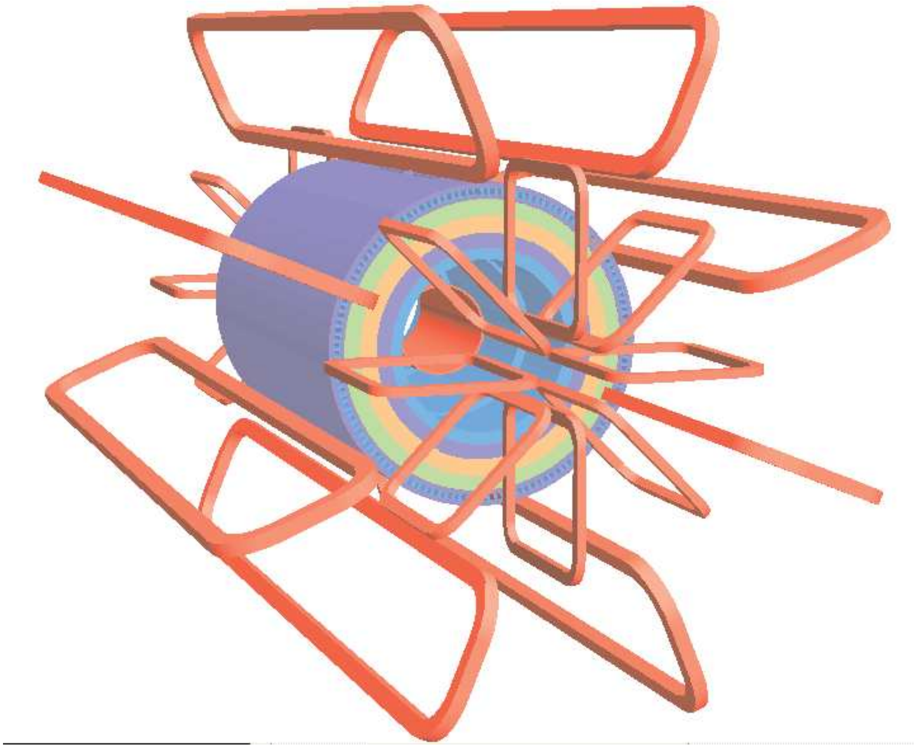

Figure 3.27: Geometry of magnet windings and tile calorimeter iron

Central solenoid

Centra solenoid is aligned on the beam axis and provides 2 T axial magnetic field for inner detector. It was designed to keep the material thickness in front of the calorimeter as low as possible (∼0.66 radiation length at normal incidence). The solenoid is charged and discharged in about 30 minutes.

Barrel toroid

Barrel toroid surrounds the calorimeters and both end-caps toroids. It generates magnetic field of approximately 0.5 T in central region of the muon spectrometer. It consists of eight coils encased in individual racetrack-shaped, stainless-steel vacuum vessels. Coils are assembled radially and symmetrically around the beam axis.

End-cap toroids

End-caps toroids are inserted in barrel toroid at each end. They consist of eight racetrack-like, double-pancake-shaped coils. They generate magnetic field of approximately 1 T for the muon spectrometer in end-caps region. Coils of end-caps magnets are rotated by 22.5° with respect to barrel toroid coils

3.6.2 Forward detectors

There are three smaller detector systems covering the forward region of ATLAS detector - LUCID, ALFA and ZDC.

LUCID

LUCID (LUminosity measurement using Cerenkov Integrating Detector) is Cerenkov detector online monitoring relative luminosity in ATLAS. It is closest to the interaction point.

ALFA

ALFA (Absolute Luminosity For ATLAS) consists of scintillating fibre trackers located inside Roman pots. It determines absolute luminosity in ATLAS.

ZDC

ZDC (Zero-Degree Calorimeter) modules consist of layers of alternating quartz rods and tungsten plates. It determines centrality in heavy-ion collisions.

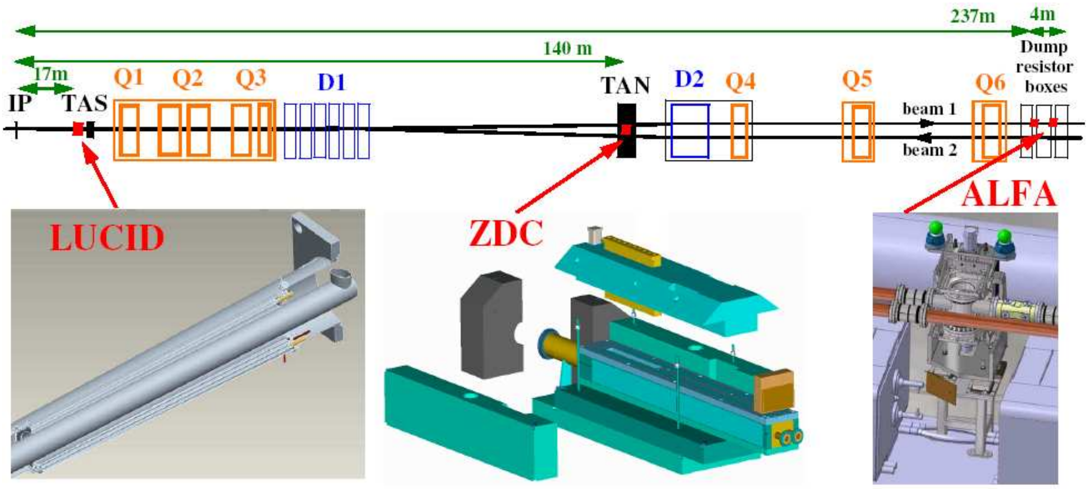

Figure 3.28: Placement of the forward detectors along the beam-line around the ATLAS interaction point

3.6.3 Beam pipe

Beam pipe in ATLAS experimental area is 38 m long and consists of seven parts. Inside is ultra-high vacuum. The central chamber (vacuum inner detector) is centered about the interaction point. It has a 58 mm inner diameter. The remaining six chambers are installed symmetrically on both sides of the interaction point. They are tubes with diameters 60 mm, 80 mm and 120 mm on each side.

Chapter 4

E-p scale

4.1 Determination of the mass scale

At first, it is necessary to clarify the term mass scale. Mass scale is proportionality coefficient between the measured and the truth value of the mass of investigated particle (and mass is mean value of mass distribution). This part is compilation from source [5].

Determination of the mass scale is necessary for determination of a measurement accuracy in ATLAS experiment. Knowledge of the mass scale and rising of accuracy of the mass measurement is important for many models of elementary particles physics. For example

- measurement of the Higgs boson mass can be known with statistical accuracy ~ 0.1 % over a wide range of Higgs boson masses. It will provide strong additional constraint for Standard Model.
- precision measurements of masses of various supersymmetrical particles (if they will be discovered on LHC)
- very precise measurements of the masses of the W boson and of the top quark. It will provide strong additional constraint for Standard Model.

It leads to following requirements for the knowledge of absolute scale of energy and momentum measurements

- electrons and muons - scale should be known to an accuracy of ~ 0.1 % (for the measurements of the W boson mass at low luminosity is required accuracy at the level of 0.02 %)
- hadronic jets - scale should be known to an accuracy of ~ 1 % (in fact, it cannot be decreased below the level of 1 % because of uncertainties caused by fragmentation and hadronisation of the original parton)

When first LHC collision will be recorder in the detector, the knowledge of the absolute calibration of the various system in ATLAS will be

- 0.5 % for the absolute momentum scale for charged particles measured in the Inner Detector and the Muon system
- $1 - 2$ % for the absolute scale for electrons and photons
- $\sim 5 - 10$ % for the absolute energy scale for hadronic jets over $|\eta| < 3.2$

This initial knowledge needs to be improved by factor of ~ 25 for electrons and muons and by factor of $\sim 5-10$ for hadronic jets. The W boson mass will be known to an accuracy of $\sim 5\times10^{-4}$ and the Z boson mass with accuracy of better than $\sim 10^{-4}$.

The best accuracy on the overall mass scale will be achieved by requiring of the combinations of the information from different detectors.

- the electron energy measurements will rely on the EM calorimeter, but will be constrained by measurements in Inner Detector
- the muon momentum measurements will rely on the measurements in the Inner Detector and in the Muon system
- the hadronic jets energy measurements will rely on calorimetry over the range $|\eta| < 3.2$

In the end, all various constraints will be combined and determine one mass scale for whole ATLAS experiment.

4.1.1 Inner detector

The Momentum scale in the Inner Detector should be known to an accuracy of 0.02 % (because of the W boson mass measurement). The implications of these requirements can be summarized as follows:

- local alignment must be understood locally to $\sim 1\ \mu m$ on average in the bending plane
- the solenoidal magnetic field must be understood locally to better than 0.1 % on average
- the amount of material in the Inner Detector must be understood globally to ~ 1 % of its value
- the Inner detector p_T resolution must be understood globally to ~ 1 %

The calibration will come from the use of the mass constraint in $Z \longrightarrow \mu\mu$ decays.

4.1.2 Electromagnetic calorimetry

The electron energy scale

Required accuracy will be 0.1 % (0.02 % for low luminosity). The $Z \longrightarrow ee$ decays was used for the energy scale calibration.

The photon energy scale

Required accuracy will be 0.1 %. Possibly the only clean source of event which could be used to constraint the photon energy scale consists of $Z \longrightarrow ee\gamma$ decays. There is high p_T photon well separated from electrons.

4.1.3 Muon momentum scale

The Muon system will provide high-precision muon momentum measurement. The momentum resolution and the absolute calibration of the Muon system depends on

- the alignment of the precision chambers
- the knowledge of the magnetic field
- the knowledge of the muon energy loss in calorimeters

The track curvature measurement is obtained from three points. The $Z \longrightarrow \mu\mu$ decays was used for the momentum scale calibration.

4.1.4 Jet and E_T^{miss} scale

Jets and E_T^{miss} scale is determined by calorimeters.

Jets

Jet spectroscopy is a rather complex issue. It is subject to both physical and detector effects. The calibrations of the absolute jet energy scale is performed with

- light quarks jets - $W \longrightarrow jj$ decays from top quark decay
- events containing Z boson decaying to leptons and one high-p_T jet. This also will be very helpful to cross-check the calibration of the jet energy scale performed with $W \longrightarrow jj$ decays

E_T^{miss}

Once the absolute energy scale of the Hadronic calorimeter has been set to $\pm 1\,\%$ over $|\eta| < 3.2$, the knowledge of the absolute energy scale over the full pseudorapidity coverage is mainly of interest of physics involving an accurate measurement of E_T^{miss} (e.g. in heavy Higgs boson searches).

4.2 Electron and photon reconstruction and identification

Electrons and photons need to be reconstructed with high efficiency and accuracy. It is necessary to know calibration and expected performance of the electromagnetic calorimeter, electron and photon identification, etc. This part is compilation from source [1].

The large amount of material is in front of the electromagnetic calorimeter. It leads to substantial energy losses for electrons and to a large fraction of photons converting. Electron and photon reconstruction is seeded using a *sliding-window algorithm*. There is chosen a window in the middle layer of the electromagnetic calorimeter. A cluster of fixed size is then reconstructed around this seed. For electrons, the energy in the barrel is collected over 3×7 cells. For unconverted photons, it is 3×5 cells in the middle layer (converted photons are treated like electrons). For the end-cap, the area is 5×5 cells in layer 2 for electrons and photons.

The seed cluster is taken from the electromagnetic calorimeter and a loosely matching track is searched for amongst all reconstructed tracks. Electrons and photons are separated reasonably cleanly (because of electron has an associated track but no associated conversion). For all candidates are calculated shower-shape variables (lateral and longitudinal shower profiles, etc.), etc.

4.2.1 Electrons

The standard identification for isolated high-p_T electron is based on cuts on the shower shapes, on information from the reconstructed track and on the combined reconstruction. There are three sets of cuts:

1. loose cuts - consisting of simple shower-shape cuts and very loose matching cuts between reconstructed track and calorimeter cluster
2. medium cuts - adds shower-shape cuts using the information from first layer of the electromagnetic calorimeter and track-quality cuts
3. tight cuts - tighten the track-matching criteria and the cut on the energy-to-momentum ratio. These cuts requires the presence of a vertexing-layer hit on the track and a high ratio between high-threshold and low-threshold hits in the TRT. There are two sets of tight selection cuts
    - tight(TRT) - there is applied TRT cut with approximately 90 % efficiency
    - tight(isol.) - there is applied TRT cut with approximately 95 % efficiency in combination with calorimeter isolation cut

4.2.2 Photons

Photons are harder to extract as a signal. There has been optimised a single set of photon identification cuts (similar to the "tight cuts" for electron). There has been also added a simple track-isolation criterion.

Chapter 5

Physics on ATLAS

5.1 Physics program

There are several different models of elementary particles and their interactions. It is assumed, that with data from the ATLAS experiment, it will be possible to decide which model describes the physics most accurately. This part is compilation from source [6].

5.1.1 Physics models

The Standard Model is based on quantum field theory which describes the interactions of spin-1/2 point-like fermions, whose interactions are mediated by spin-1 gauge bosons. The symmetry group of the theory is $SU(3) \times SU(2) \times U(1)$. The $SU(2) \times U(1)$ symmetry group describes electroweak interaction and $SU(3)$ group describes the strong interaction (quantum chromodynamics or QCD). The Standard Model is successful even at the smallest scales (10^{-18} m) and highest energies ($\sim$200 GeV).

Higgs boson

The electroweak interaction is mediated by photon γ (which has zero mass) and by three weak bosons $W^{\pm}$ and Z (which have non-zero mass). This is possible only if the symmetry group $SU(2) \times U(1)$ is spontaneously broken (Higgs mechanism). As a consequence of this mechanism is the prediction of the Higgs boson. The Higgs boson mass is one of parameters of the Standard Model. The Higgs boson mass doesn't arise from the Standard Model, but some constraints can be delivered from perturbative calculations within the model. Upper limit estimation for the Higgs boson mass is 800 GeV.

Hard interactions of quarks and gluons

Scattering processes at high energy hadron colliders can be classified as either hard or soft. Results of hard processes can be predicted with perturbative QCD. But soft processes are dominated by non-perturbative QCD effects. Generic hard scattering process is depicted in Figure 5.1. This part is compilation from source [8].

Formalisms: One of the most important quantities in particle physics is cross section. Hadronic cross section $\sigma(AB \longrightarrow \mu^+\mu^- + X)$ is equal to:

$$\sigma_{AB} = \int dx_a dx_b f_{a/A}(x_a, Q^2) f_{b/B}(x_b, Q^2) \hat{\sigma}_{ab \longrightarrow X} \tag{5.1}$$

where $f_{a/A}$, $f_{b/B}$ are parton distribution functions extracted from deep inelastic scattering, Q^2 is a large momentum scale that characterizes the hard scattering and $\hat{\sigma}_{ab \longrightarrow X}$ is microscopic

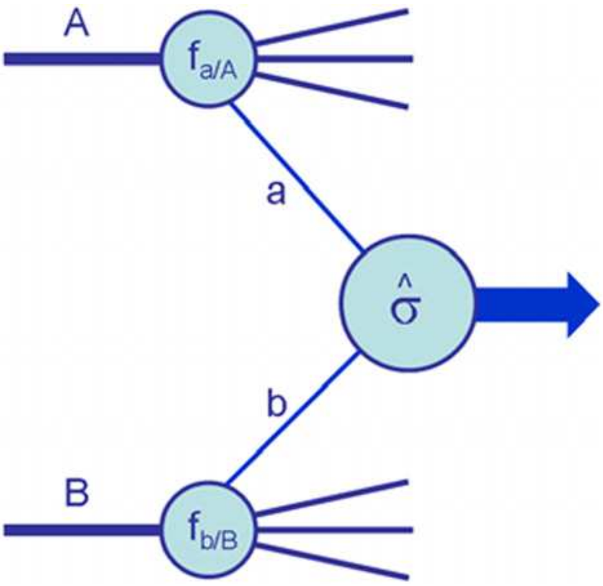

Figure 5.1: Diagrammatic structure of a generic hard scattering process

cross section for Drell-Yan process, i.e. process of production of a massive lepton pair by quark-antiquark annihilation ($X = l^+l^-$ is lepton pair; $ab = q\bar{q}$ or $\bar{q}q$). Now it is possible to express 5.1 perturbatively as

$$\sigma_{AB} = \int dx_a dx_b f_{a/A}(x_a, \mu_F^2) f_{b/B}(x_b, \mu_R^2) \times [\hat{\sigma}_0 + \alpha_S(\mu_R^2)\hat{\sigma}_1 + \ldots]_{ab \longrightarrow X} \tag{5.2}$$

where μ_F is factorization scale and μ_R is renormalization scale. For Drell-Yan processes, the standard choice is $\mu_F = \mu_R = M$ the mass of lepton pair.

Drell-Yan process: In Drell-Yan process, quark and antiquark annihilate to produce a virtual photon.

$$q\overline{q} \longrightarrow \gamma^* \longrightarrow l^+l^-$$

If the centre-of-mass energy is sufficient, then W and Z boson can be produced as well.

Such cross section is obtained from fundamental QED, with the addition of the appropriate color and charge factors as

$$\sigma(q\bar{q} \longrightarrow e^+e^-) = \frac{4\pi\alpha^2}{3\hat{s}} \frac{1}{N} Q_q^2 \tag{5.3}$$

where Q_q is quark charge, 1/N=1/3 is color factor and $\sqrt{\hat{s}}$ is centre-of-mass energy. Then, in centre-of-mass frame, the differential cross section will be

$$\frac{d\widehat{\sigma}}{dM^2} = \frac{\widehat{\sigma}_0}{N} Q_q^2 \delta(\widehat{s} - M^2) \tag{5.4}$$

where M is the mass of the lepton pair and

$$\widehat{\sigma}_0 = \frac{4\pi\alpha^2}{3M^2}$$

In centre-of-mass frame fourmomenta of incoming partons will be

$$\begin{aligned} p_1^\mu &= \frac{\sqrt{s}}{2}(x_1, 0, 0, x_1) \\ p_2^\mu &= \frac{\sqrt{s}}{2}(x_2, 0, 0, -x_2) \end{aligned}$$

where

$$x_1 = \frac{M}{\sqrt{s}}\, e^{y} \qquad x_2 = \frac{M}{\sqrt{s}}\, e^{-y}$$

where y is rapidity. The differential cross section is therefore

$$\frac{d\sigma}{dM^2dy} = \frac{\widehat{\sigma}_0}{N_s}\sum_k Q_k^2(q_k(x_1,M^2)\overline{q}_k(x_2,M^2) + [1 \longleftrightarrow 2]) \tag{5.5}$$

Furthermore, subprocess cross sections for W and Z productions are

$$\sigma(q\bar{q}' \longrightarrow W) = \frac{\pi}{3}\sqrt{2}G_F M_W^2 |V_{qq'}|^2 \delta(\hat{s} - M_W^2) \tag{5.6}$$

$$\sigma(q\bar{q} \longrightarrow Z) = \frac{\pi}{3}\sqrt{2}G_F M_Z^2 (v_q^2 + a_q^2)\delta(\hat{s} - M_Z^2) \tag{5.7}$$

where $V_{qq'}$ is appropriate Cabibbo-Kobayashi-Maskawa matrix element, v_q is vector and a_q is axial vector of coupling of the Z boson to the quarks. These formulae are valid, when decay width of the gauge boson is neglected.

SUSY theory

Supersymmetry is one of very few mechanisms for incorporating gravity into the quantum theory of particle interactions. This model postulates the existence of superpartners for all presently observed particles. Bosonic superpartners of fermions are squarks and sleptons. Fermionic superpartners of bosons are gluinos and gauginos. There are also multiple Higgs bosons - $h, H, A, H^{\pm}$. Thus, there are many unobserved particles. Their properties are calculable in the theory given certain parameters. Unfortunately these parameters are unknown. If the SUSY theory is to have anything to do with electroweak symmetry breaking, the masses should be in the region below or order of 1 TeV. There is so far no experimental evidence for this theory.

Technicolor theory

It is model based on dynamical symmetry breaking. It assumes the existence of technifermions possessing a technicolor charge and interacting strongly at a high scale. If the dynamics is to have anything to do with electroweak symmetry breaking, new states would be in the region below 1 TeV.

Other theories

There are more theoretical concepts which leads beyond the Standard Model. For example excited quarks, leptoquarks, new gauge bosons, right-handed neutrinos and monopoles.

5.1.2 Simulations

There are several available Monte Carlo event generators for particle interactions. The most frequently used generators are HERWIG, ISAJET and PYTHIA. Each of these simulates a hadronic final states corresponding to some particular model of the underlying physics. For the hard-scattering events ISAJET uses a pomeron model, HERWIG uses parametrisation of data (mainly from the CERN $p\overline{p}$ Collider) and PYTHIA uses mini-jet model. The Standard Model physics and Higgs searches were mostly simulated with PYTHIA. ISAJET was used for supersymmetry studies. HERWIG has been used for some of the QCD studies.

Part II

Results of analysis

Chapter 6

Results of analysis of fully reconstructed $p + p \longrightarrow X + Z \longrightarrow e^+ + e^-$ events at the 14 TeV centre of mass energy

6.1 Dataset used, investigated entities, event selection

ATLAS CSC official sample number 5144 was used [14]. It contains around 490 thousands of reconstructed events of

$$p + p \longrightarrow X + Z \longrightarrow e^+ + e^-$$

at the 14 TeV centre of mass energy. Pythia generator was used to generate events. They were reconstructed in Rel. 12.0.6.1, simulated in Rel. 12.0.3.1.3 and generated in Rel. 11.0.42.1 of ATLAS offline software. Events satisfy filtering conditions. Event is selected, if it contains at least one secondary electron with the following properties:

- $|\eta| < 2.7$
- $p_T > 10\ GeV$
- $M_{ll} > 60\ GeV$

where M_{ll} is a mass of lepton pair. Filtering efficiency is 86 % and filtered cross section is $1.432 \times 10^6\ fb$. AANT (Athena Aware NTuples) derived from AOD (Analysis Object Data) were analysed using ROOT version 5.14/00 (see [12]). These AANT contain 398750 events.

Investigated entities were

1. at generator level
   - Z boson
   - electron
   - positron
   - lepton pair
2. at level of reconstruction
   - reconstructed electron
   - reconstructed positron

- reconstructed Z boson, i.e. Z boson reconstructed from fourmomenta of reconstructed electron and positron

Three levels of event selection were used:

1. Event was selected at the first level, when one Z boson and one lepton pair are created at generator level.
2. The second level consists of events from the first level with one reconstructed Z boson. Reconstructed electron and positron are required to be "tight" according ATLAS selection criteria [2]. An electron candidate is defined "tight" when its transverse energy is above 15 GeV and satisfies the following criteria:
    - track matching
    - isolation
3. The third level consists of events from the second level with the following properties of reconstructed secondary leptons:
    - $|\eta| < 2.5$
    - $p_T > 20\, GeV$
    - $75\, GeV/c^2 < m_Z < 105\, GeV/c^2$

6.2 Results

6.2.1 Kolmogorov-Smirnov test

Kolmogorov-Smirnov test of goodness of fit (see [13]) is statistical test investigating whether two one-dimensional sets of points are compatible with coming from the same parent distribution. Following figures show dependence of the Kolmogorov probability on the number of bins for value of the E-p scale 2.00 % in mass, p_T and rapidity distributions. These are

- Values of Kolmogorov probability for mass distribution are shown in Figure 6.1. It was created by analyzing the histograms with the range (60, 200) GeV/c^2 and with the following number of bins: 56, 560, 5600, 56000, 560000.
- Values of Kolmogorov probability for mass distribution are shown in Figure 6.2. It was created by analyzing the histograms with the range (88.5, 94) GeV/c^2 and with the following number of bins: 11, 110, 1100, 11000, 110000.
- Values of Kolmogorov probability for p_T distribution are shown in Figure 6.3. It was created by analyzing the histograms with the range (0, 100) GeV/c and with the following number of bins: 50, 100, 1000, 10000, 100000.
- Values of Kolmogorov probability for rapidity distribution are shown in Figure 6.4. It was created by analyzing the histograms with the range (-3, 3) and with the following number of bins: 60, 120, 1200, 12000, 120000.

Kolmogorov probability of the mass distribution is dependent on the number of bins. Kolmogorov probability of the p_T distribution is almost independent on the number of bins. Kolmogorov probability of the rapidity distribution is independent on the number of bins. The highest number of bins was used for the Kolmogorov test.

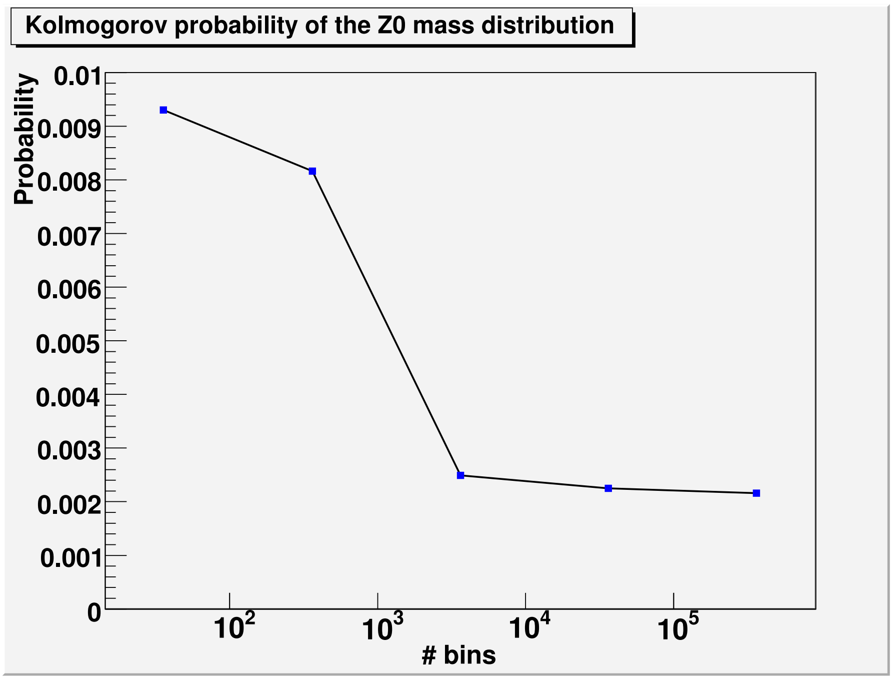

Figure 6.1: Dependence of the Kolmogorov probability on the number of bins for Z boson mass distribution. It was created by analyzing the histograms with the range (60, 200) GeV/c^2 and with the following number of bins: 56, 560, 5600, 56000, 560000.

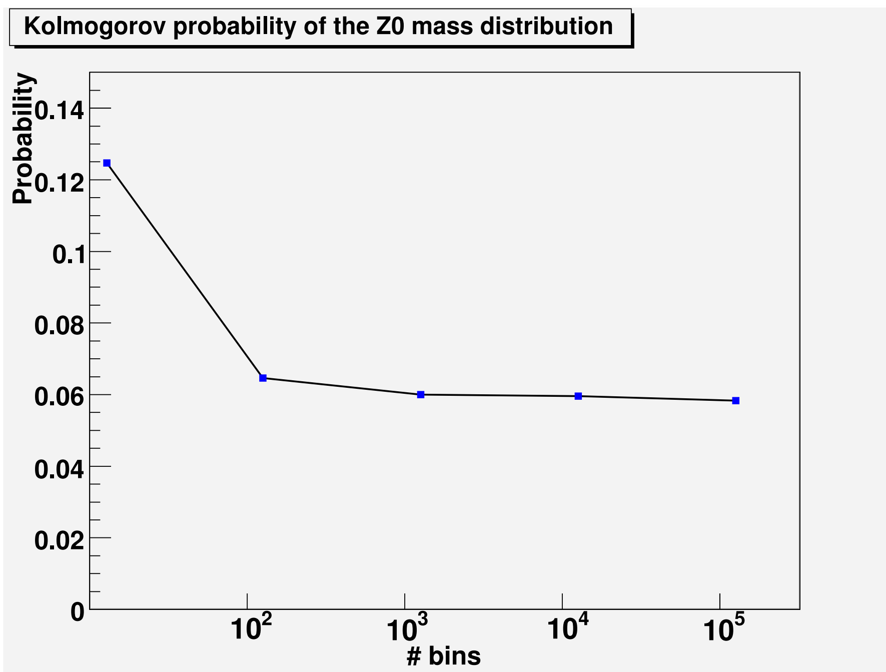

Figure 6.2: Dependence of the Kolmogorov probability on the number of bins for Z boson mass distribution. It was created by analyzing the histograms with the range (88.5, 94) GeV/c^2 and with the following number of bins: 11, 110, 1100, 11000, 110000.

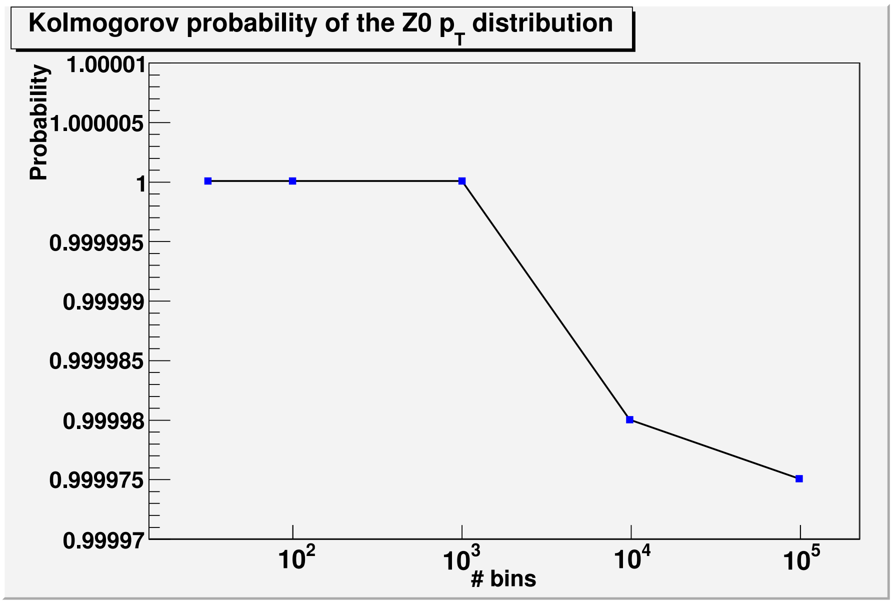

Figure 6.3: Dependence of the Kolmogorov probability on the number of bins for Z boson p_T distribution. It was created by analyzing the histograms with the range (0, 100) GeV/c and with the following number of bins: 50, 100, 1000, 10000, 100000.

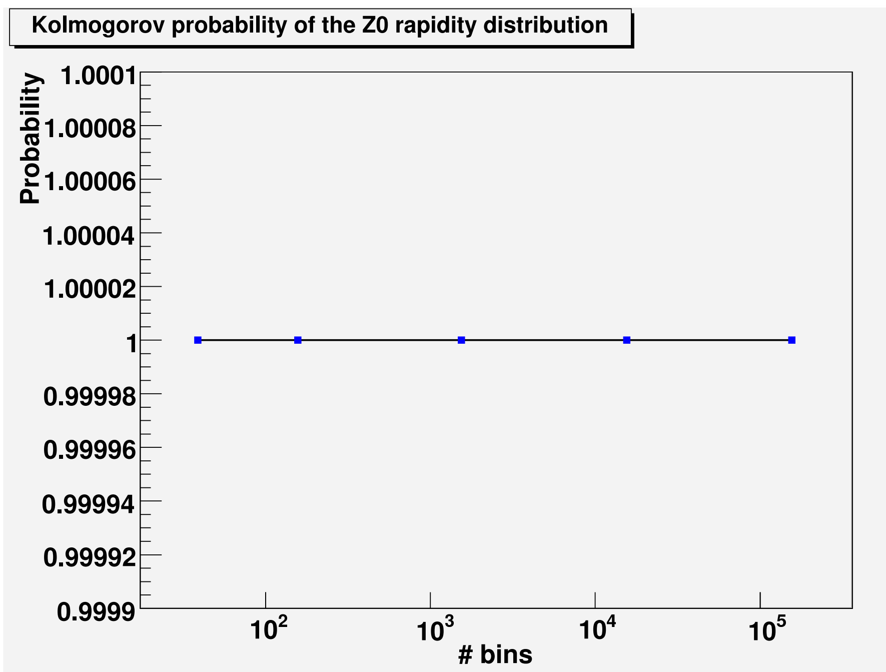

Figure 6.4: Dependence of the Kolmogorov probability on the number of bins for Z boson rapidity distribution. It was created by analyzing the histograms with the range (-3, 3) and with the following number of bins: 60, 120, 1200, 12000, 120000.

6.2.2 Levels of event selection

Number of events and corresponding cross sections in all three levels of event selection are shown in Table 6.1.

Level of event selection	Number of events	Corresponding cross section [pb]
1.	398750	1432
2.	76003	273
3.	64374	231

Table 6.1: Number of events in levels of event selection and corresponding cross sections

Corresponding cross section is calculated according to formula

$$\text{corresponding cross section} = \frac{\text{total cross section} \cdot \text{filtering efficiency} \cdot \text{number of events}}{398750}$$

where filtered cross section (total cross section · filtering efficiency) is 1432 pb.

Distributions of p_T and rapidity for all three levels of event selection are shown in Figure 6.5 and 6.6, respectively. These figures imply, that the greatest decrease of the number of events happens between first and second level of event selection.

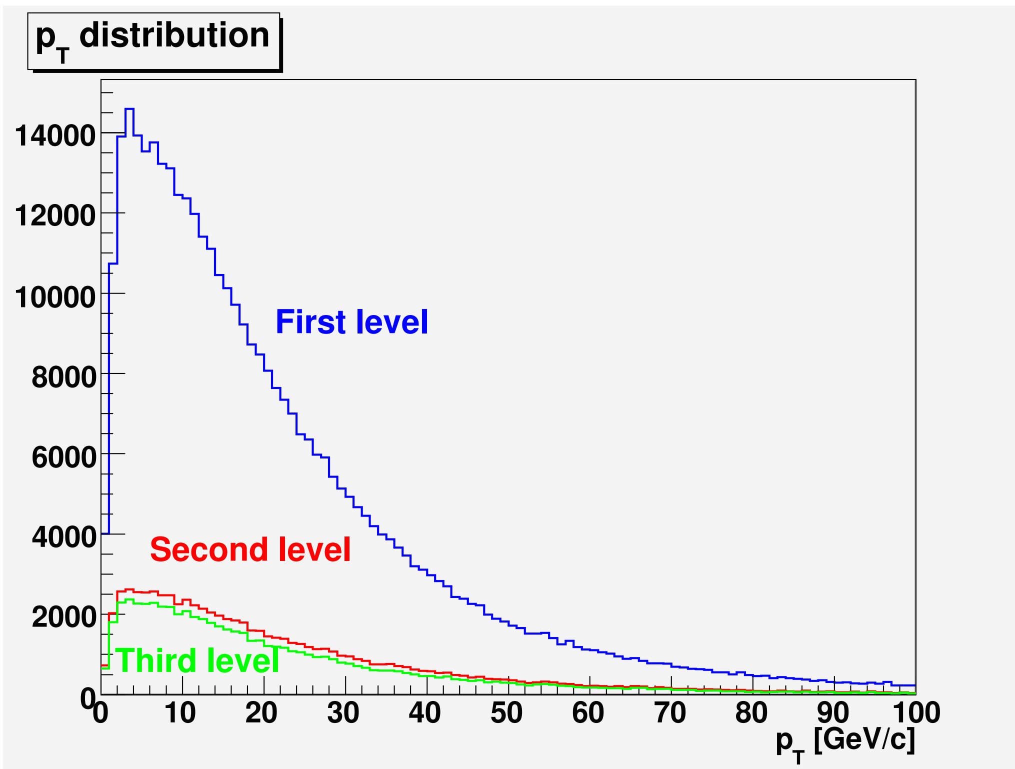

Figure 6.5: p_T distribution of lepton pair for all three levels of event selection

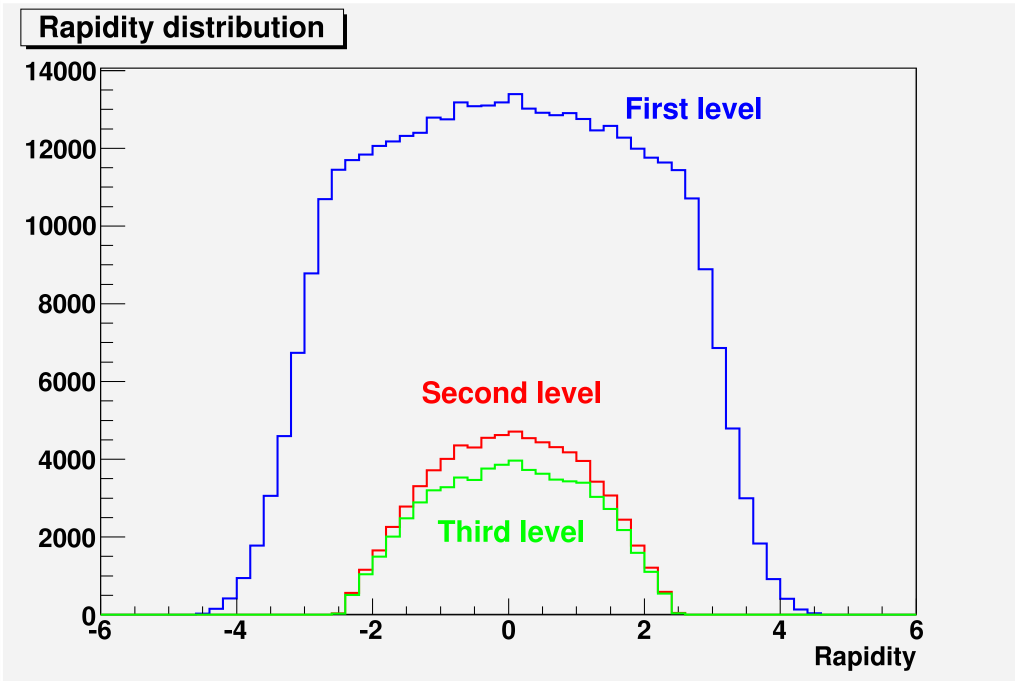

Figure 6.6: Rapidity distribution of Z boson at generator level for all three levels of event selection.

6.2.3 Influence of uncertainty of E-p scale

Before investigation of the influence, the E-p scale must be defined. Thus, *E-p scale is a proportionality coefficient between the measured and the truth value of particle's fourmomentum* (deduced from [5], 401 - 404).

At the beginning of investigation, space (η, ϕ) was divided into regions of good uniformity of response of ATLAS detector (see [5], page 135 and [1], page 330). In the concrete, it is $26(\eta) \times 17(\phi) = 442$ regions. For each of these regions is created factor $F = 1 + shift$, where $shift \in \langle -\alpha, \alpha \rangle$ and α is the value of the E-p scale uncertainty. Then fourmomentum of every electron or positron is multiplied by factor F of region where particle flights through. Influence of these fourmomentum changes is investigated.

Now follow results of E-p scale uncertainty investigation. Following ROOT files were used and analysed: caan0000.root, caan0002.root, caan0010.root, caan0020.root, caan0040.root, caan0060.root, caan0080.root, caan0100.root, caan0150.root and caan0200.root. Values of E-p scale uncertainty, number of events and corresponding cross section for each file are given in the Table 6.2. They contain data with uncertainty of E-p scale from 0 % to 2 %. Investigated interval of E-p scale uncertainty goes from the goal value (0.02 %) to the starting value (2 %) (see 4.1).

Figure 6.7 shows p_T distribution of reconstructed Z boson for the E-p scale uncertainty 0 % (blue line) and 2 % (green line).

Table 6.2 implies, that the number of events is almost independent on the E-p scale uncertainty. Figure 6.7 shows, that p_T distributions of reconstructed Z boson are almost identical.

caaanxxxx.root	E-p scale uncertainty	Number of events	Corresponding cross section [pb]
0000	0.00%	64374	231.181
0002	0.02%	64372	231.174
0010	0.10%	64364	231.145
0020	0.20%	64366	231.153
0040	0.40%	64363	231.142
0060	0.60%	64371	231.171
0080	0.80%	64378	231.196
0100	1.00%	64373	231.178
0150	1.50%	64366	231.153
0200	2.00%	64352	231.102

Table 6.2: Number of events for the third level of event selection and corresponding cross sections for all investigated values of E-p scale uncertainty.

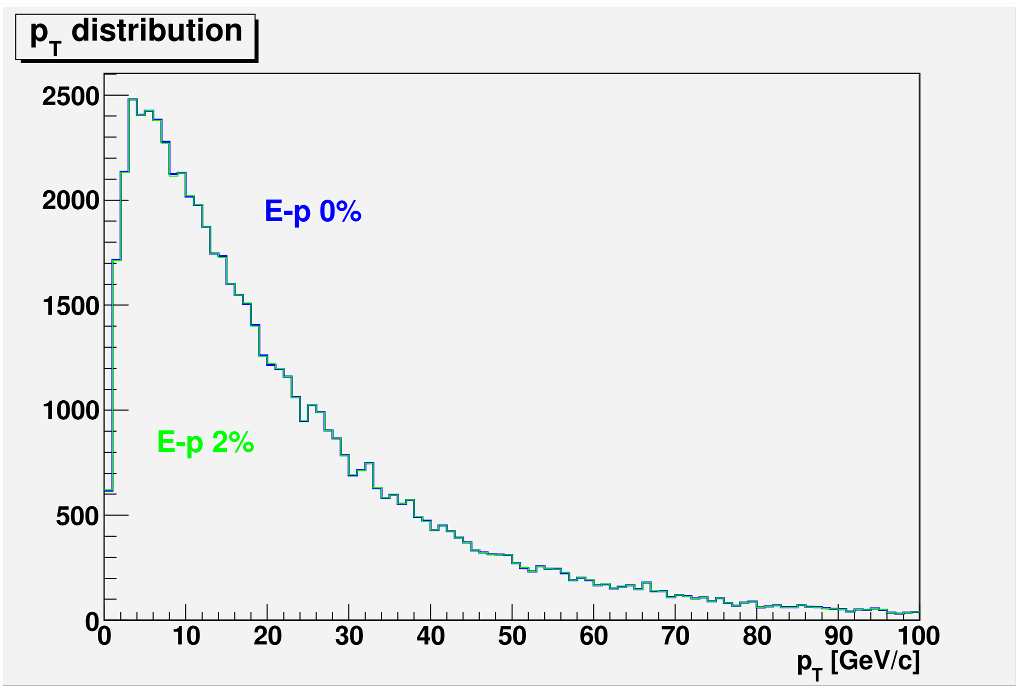

Figure 6.7: p_T distribution of reconstructed Z boson for boundary values of the E-p scale uncertainty.

6.2.4 Z boson mass distribution fitting

Here follow the results of fitting of Z boson mass distribution. Two different statistical distributions were used: Gaussian distribution and relativistic Breit-Wigner distribution (see [9]):

$$\sigma_{Gauss} \sim \frac{1}{\sqrt{2\pi}\sigma} \exp\left(-\frac{(m-M_Z)^2}{2\sigma^2}\right) \tag{6.1}$$

$$\sigma_{RBW} \sim \frac{m^2 \frac{\Gamma_0^2}{M_Z^2}}{(m^2-M_Z^2)^2 + m^4 \frac{\Gamma_0^2}{M_Z^2}} \tag{6.2}$$

where σ is the standard deviation, M_Z is mean value of Z boson mass distribution and Γ_0 is full width at half maximum (FWHM). For comparison it is necessary to tramsform standard deviation of the Gaussian distribution into FWHM. It is done by following formula

$$\Gamma_0 = 2\sqrt{2\ln 2}\sigma$$

Now follow the results of Z boson mass fitting.

Different phases od simulation

Here follow the results of fitting from the generation to the reconstruction. Results for Gaussian distribution are collected in Table 6.3.

h0xxxx	p0	p1	p1$\cdot 2\sqrt{2\ln 2}$	p2	χ^2/NDF
h01001	$2.065 \times 10^5 \pm 413$	1.296 ± 0.003	3.051 ± 0.007	91.13 ± 0.00	2152/7
h01101	$1.700 \times 10^5 \pm 399$	1.420 ± 0.004	3.344 ± 0.010	90.91 ± 0.00	1509/7
h02001	$3.946 \times 10^4 \pm 181$	1.298 ± 0.007	3.056 ± 0.017	91.13 ± 0.01	440.7/7
h02101	$3.422 \times 10^4 \pm 178$	1.412 ± 0.010	3.324 ± 0.022	90.92 ± 0.01	337/7
h02301	$3.614 \times 10^4 \pm 543$	2.359 ± 0.042	5.555 ± 0.098	90.13 ± 0.03	7.371/7
h03001	$3.539 \times 10^4 \pm 171$	1.297 ± 0.008	3.054 ± 0.018	91.14 ± 0.01	398/7
h03101	$3.130 \times 10^4 \pm 170$	1.412 ± 0.010	3.326 ± 0.027	90.93 ± 0.01	320.3/7
h03301	$3.347 \times 10^4 \pm 508$	2.337 ± 0.042	5.503 ± 0.099	90.15 ± 0.03	6.152/7

Table 6.3: Results of the Gaussian fit

In this part, parameter p0 is normalization, p1 is FWHM (standard deviation) and p2 is mass. In the Table 6.3, p1 is standard deviation and thus p1$\cdot 2\sqrt{2\ln 2}$ is FWHM. In the Table 6.4, parameter p1 is FWHM.

These parameters result from the fit of the following histograms:

- h01001 is a histogram of generated mass of the Z boson in the first level of event selection
- h01101 is a histogram of generated mass of lepton pair in the first level of event selection
- h02001 is a histogram of generated mass of the Z boson in the second level of event selection
- h02101 is a histogram of generated mass of lepton pair in the second level of event selection
- h02301 is a histogram of reconstructed mass of Z boson in the second level of event selection
- h03001 is a histogram of generated mass of the Z boson in the third level of event selection
- h03101 is a histogram of generated mass of lepton pair in the third level of event selection

- h03301 is a histogram of reconstructed mass of Z boson in the third level of event selection

They all have range (0, 200) GeV/c^2 and 400 bins. Results of Breit-Wigner fit are collected in the Table 6.4.

h0xxxx	p0	p1	p2	χ^2/NDF
h01001	$4.147 \times 10^8 \pm 1.252 \times 10^6$	2.535 ± 0.009	91.16 ± 0.00	$63.32/7$
h01101	$3.024 \times 10^8 \pm 1.027 \times 10^6$	2.917 ± 0.013	90.94 ± 0.00	$732.5/7$
h02001	$7.912 \times 10^7 \pm 5.449 \times 10^5$	2.540 ± 0.022	91.15 ± 0.01	$20.86/7$
h02101	$6.142 \times 10^7 \pm 4.650 \times 10^5$	2.886 ± 0.029	90.94 ± 0.01	$145.8/7$
h02301	$3.601 \times 10^7 \pm 2.830 \times 10^5$	5.494 ± 0.107	90.20 ± 0.02	$41.19/7$
h03001	$7.100 \times 10^7 \pm 5.188 \times 10^5$	2.539 ± 0.023	91.16 ± 0.01	$16.16/7$
h03101	$5.619 \times 10^7 \pm 4.454 \times 10^5$	2.887 ± 0.030	90.95 ± 0.01	$130.9/7$
h03301	$3.366 \times 10^7 \pm 2.741 \times 10^5$	5.452 ± 0.108	90.22 ± 0.03	$40.07/7$

Table 6.4: Results of the relativistic Breit-Wigner fit

In the following figures is shown the evolution of mass distribution and fit parameters (mean value, FWHM, χ^2/NDF) for generated Z boson, lepton pair, reconstructed Z boson and reconstructed Z boson with E-p scale uncertainty 2.00 % on the third level of event selection.

Figure 6.9 of mass distribution shows that relativistic Breit-Wigner distribution is closer to correct value [9] from generation to reconstruction. FWHM (Figure 6.10) increases in similar way both for the relativistic Breit-Wigner and Gaussian distribution from generation to reconstruction. Figure 6.11 of χ^2/NDF shows that relativistic Breit-Wigner distribution is better fit for generated entities, but for reconstructed entities is better Gaussian fit.

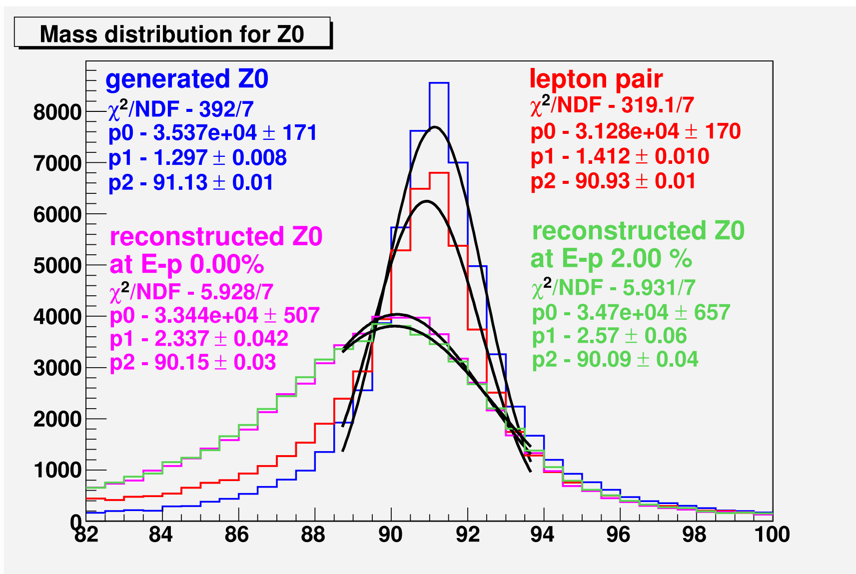

Figure 6.8: Mass distribution of generated Z boson, lepton pair, reconstructed Z boson and reconstructed Z boson with E-p scale uncertainty 2.00 % on the third level of event selection

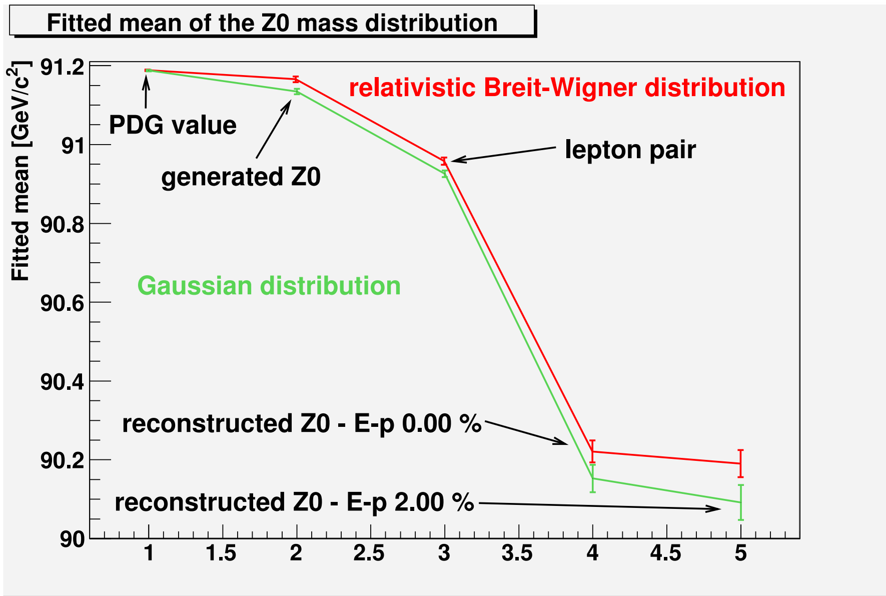

Figure 6.9: Fitted mean value of Z boson mass distribution for generated Z boson, lepton pair, reconstructed Z boson and reconstructed Z boson with E-p scale uncertainty 2.00 % on the third level of event selection

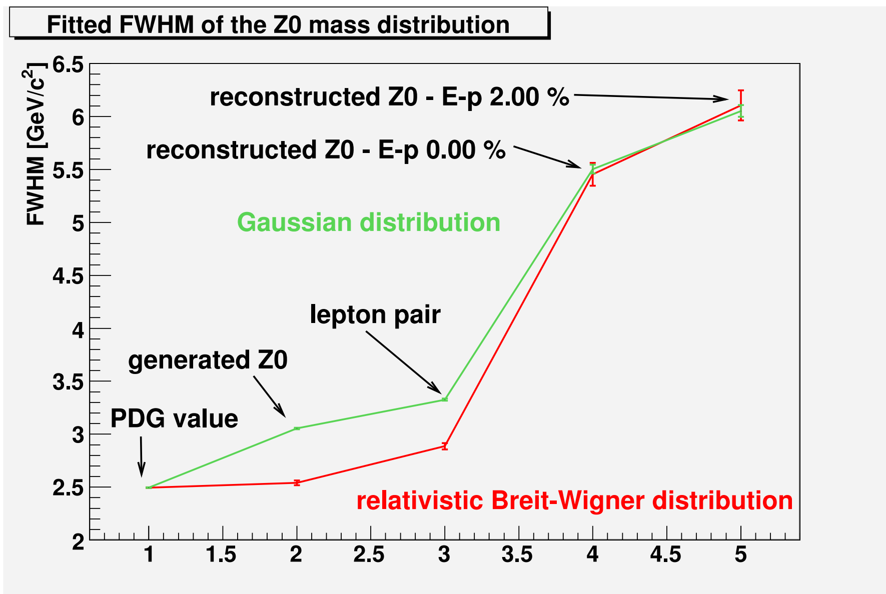

Figure 6.10: FWHM of Z boson mass distribution for generated Z boson, lepton pair, reconstructed Z boson and reconstructed Z boson with E-p scale uncertainty 2.00 % on the third level of event selection

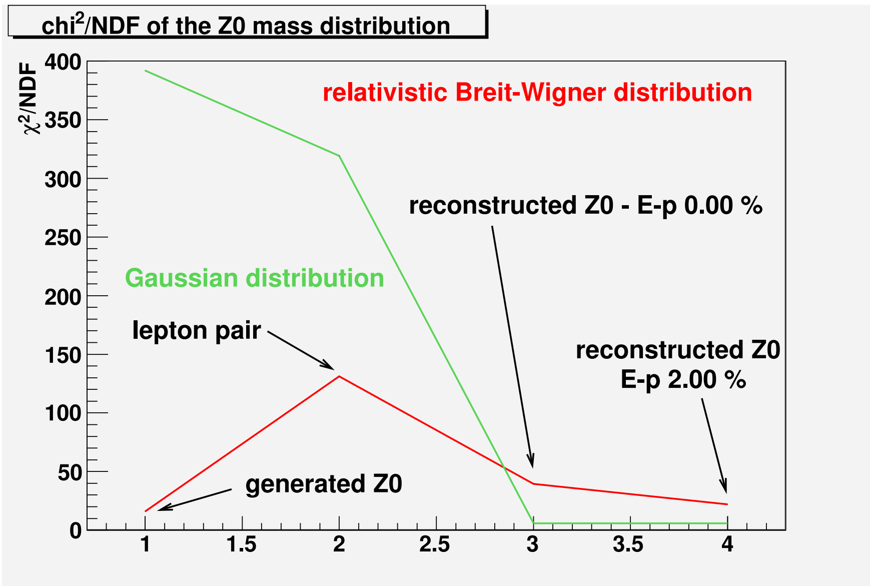

Figure 6.11: χ^2/NDF of Z boson mass distribution for generated Z boson, lepton pair, reconstructed Z boson and reconstructed Z boson with E-p scale uncertainty 2.00 % on the third level of event selection

Dependence on the E-p scale uncertainty

From this point on, different set of histograms is analysed. These are histograms of mass, p_T and rapidity of the reconstructed Z boson on the third level of event selection.

- h02301 is a histogram of mass distribution with non-zero uncertainty of the E-p scale. It has range (0, 200) GeV/c^2 and 400 bins.
- h02302 is a histogram of p_T distribution with non-zero uncertainty of the E-p scale. It has range (0, 100) GeV/c and 50 bins.
- h02303 is a histogram of rapidity distribution with non-zero uncertainty of the E-p scale. It has range (-3, 3) and 60 bins.
- h2301a_kol is a histogram of mass distribution with uncertainty of the E-p scale 0.00 % (used for Kolmogorov-Smirnov test). It has range (60, 200) GeV/c^2 and 560000 bins.
- h2301b_kol is a histogram of mass distribution with uncertainty of the E-p scale 0.00 % (used for Kolmogorov-Smirnov test). It has range (88.5, 94) GeV/c^2 and 110000 bins.
- h2302_kol is a histogram of p_T distribution with uncertainty of the E-p scale 0.00 % (used for Kolmogorov-Smirnov test). It has range (0, 100) GeV/c and 100000 bins.
- h2303_kol is a histogram of rapidity distribution with uncertainty of the E-p scale 0.00 % (used for Kolmogorov-Smirnov test). It has range (-3, 3) and 120000 bins.
- h02301a_kol is a histogram of mass distribution with non-zero uncertainty of the E-p scale (used for Kolmogorov-Smirnov test). It has range (60, 200) GeV/c^2 and 560000 bins.

- h02301b_kol is a histogram of mass distribution with non-zero uncertainty of the E-p scale (used for Kolmogorov-Smirnov test). It has range (88.5, 94) GeV/c^2 and 110000 bins.
- h02302_kol is a histogram of p_T distribution with non-zero uncertainty of the E-p scale (used for Kolmogorov-Smirnov test). It has range (0, 100) GeV/c and 100000 bins.
- h02303_kol is a histogram of rapidity distribution with non-zero uncertainty of the E-p scale (used for Kolmogorov-Smirnov test). It has range (-3, 3) and 120000 bins.

Each of these histograms was created 100 times, each time with different configuration of the random number generator. In each loop, histogram h02301 was fitted by Gaussian and Breit-Wigner distribution and fit parameters were read-out. From histograms h02302 and h02303 were read-out mean values and RMSs. Histograms h2301a_kol, h2301b_kol, h2302_kol, h2303_kol, h02301a_kol, h02301b_kol, h02302_kol, h02303_kol were used for Kolmogorov-Smirnov test and Kolmogorov probability was read-out.

Value of each of these read-out parameters was put in histogram in each loop. Thus, histograms with 100 entries were created, each of them containing the distribution of read-out parameter. Following figures were created with mean value of parameter distribution as y-value and RMS of parameter distribution as y-errorbar. Meaning of the y-errorbar is evident. It is the spread of the investigated quantity caused by the uncertainty of the E-p scale.

Figure 6.12 of mass distribution shows, that relativistic Breit-Wigner distribution is closer to correct value of Z boson mass for all investigated values of the E-p scale uncertainty. The FWHM (Figure 6.13) of both relativistic Breit-Wigner and Gaussian distribution increases for all investigated values of the E-p scale uncertainty and is almost the same. Figure 6.14 of χ^2/NDF implies, that Gaussian distribution fits reconstructed mass of Z boson better than relativistic Breit-Wigner distribution for all investigated values of the E-p scale uncertainty. Figures of Kolmogorov probability (6.15 and 6.16) show, that probability drops with E-p scale uncertainty.

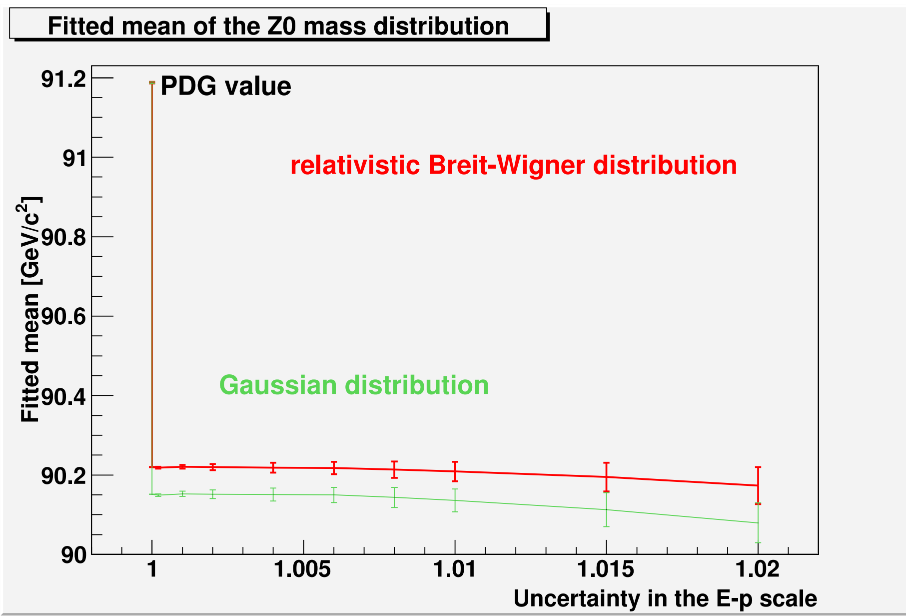

Figure 6.12: Fitted mean value of Z boson mass distribution for all investigated values of the E-p scale uncertainty. Relativistic Breit-Wigner and Gaussian fit was used. It was created by analyzing the histograms with range (0, 200) GeV/c^2 and 400 bins.

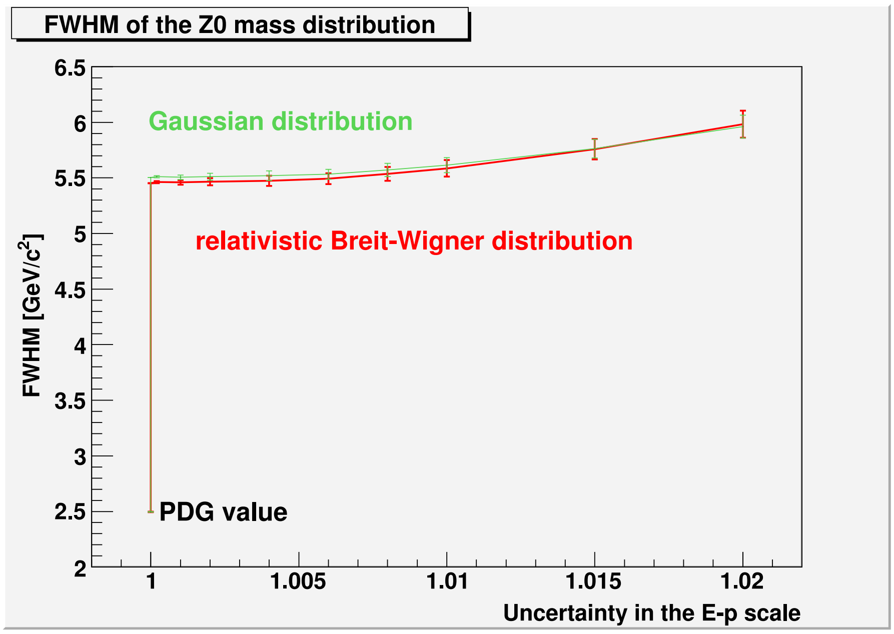

Figure 6.13: FWHM of Z boson mass distribution for all investigated values of the E-p scale uncertainty. Relativistic Breit-Wigner and Gaussian fit was used. It was created by analyzing the histograms with range (0, 200) GeV/c^2 and 400 bins.

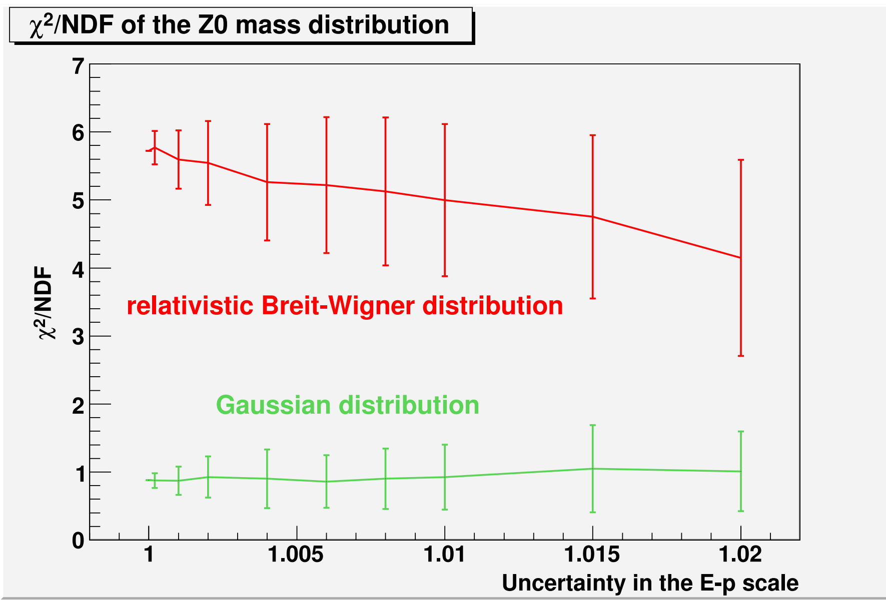

Figure 6.14: χ^2/NDF of Z boson mass distribution for all investigated values of the E-p scale uncertainty. Relativistic Breit-Wigner and Gaussian fit was used. It was created by analyzing the histograms with range (0, 200) GeV/c^2 and 400 bins.

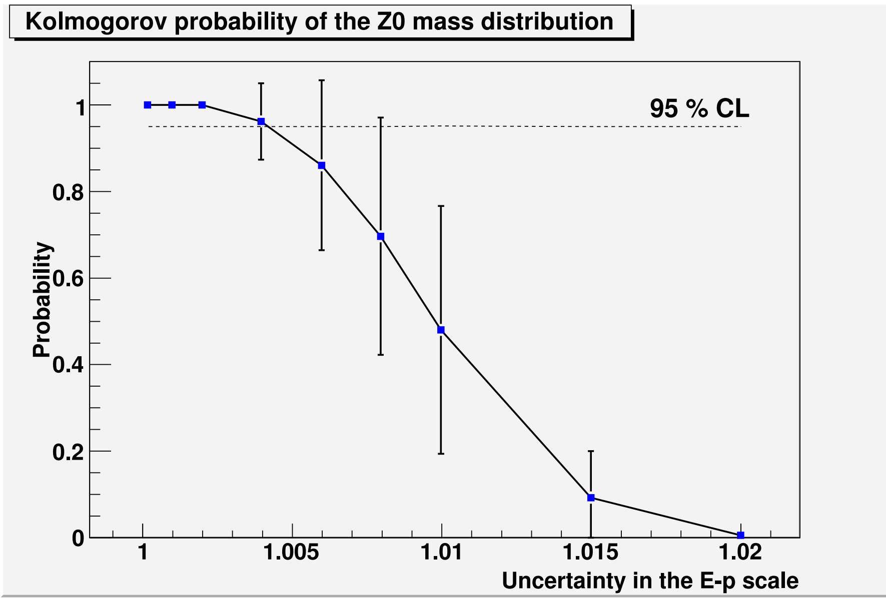

Figure 6.15: Dependence of the Kolmogorov probability on the E-p scale uncertainty for mass distribution. It was created by analyzing the histograms with range (60, 200) GeV/c^2 and 560000 bins.

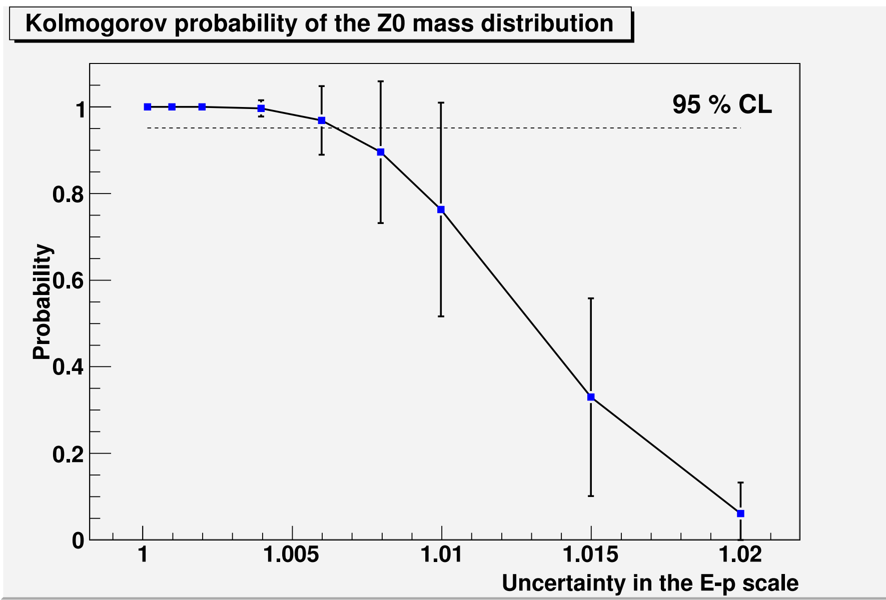

Figure 6.16: Dependence of the Kolmogorov probability on the E-p scale uncertainty for mass distribution. It was created by analyzing the histograms with range (88.5, 94) GeV/c^2 and 110000 bins.

6.2.5 Z boson p_T distribution

Now the Z boson p_T distribution has turn. Following figures show dependence of mean value, RMS and Kolmogorov probability on uncertainty of the E-p scale.

Figure 6.17 shows, that mean value of p_T distribution slightly increases for most of investigated values of the E-p scale uncertainty. RMS values (Figure 6.18) decrease for most of investigated values of the E-p scale uncertainty. Kolmogorov probability (Figure 6.19) remains constant and equal to one for almost all investigated values of the E-p scale uncertainty. Only for highest values it slightly decreases.

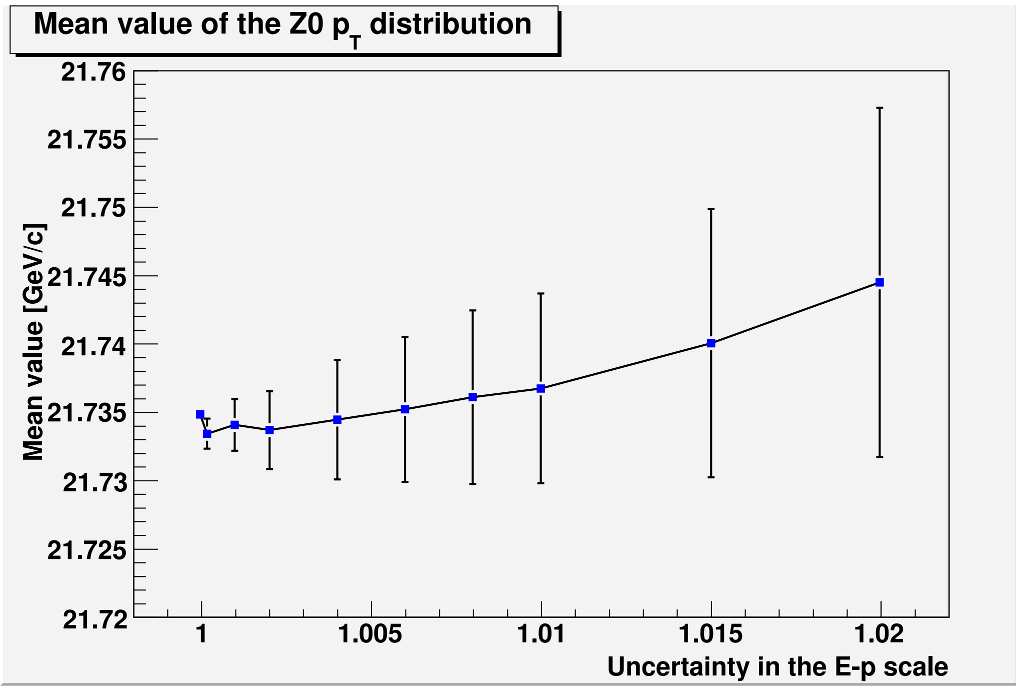

Figure 6.17: Mean value of the Z boson p_T distribution for all investigated values of the E-p scale uncertainty. It was created by analyzing the histograms with range (0, 100) GeV/c and 50 bins.

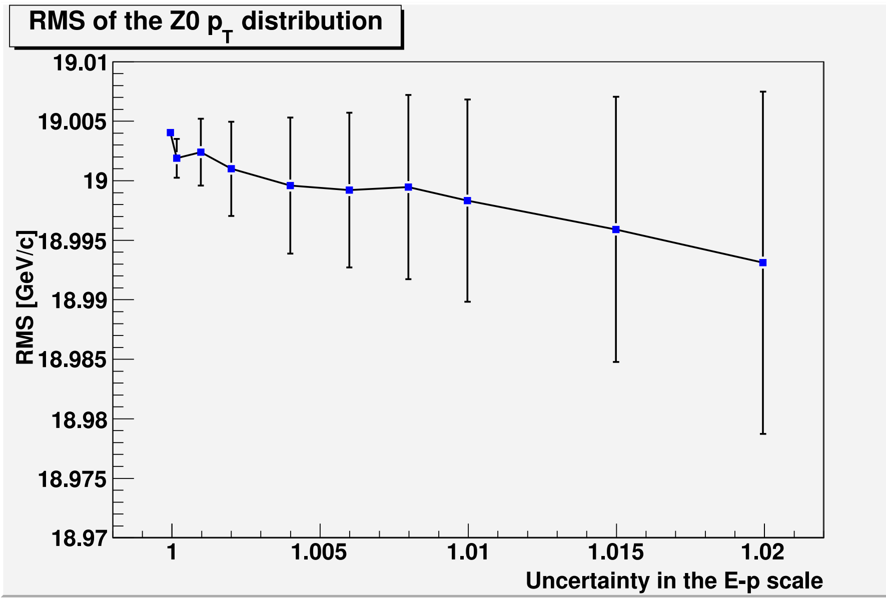

Figure 6.18: RMS of the Z boson p_T distribution for all investigated values of the E-p scale uncertainty. It was created by analyzing the histograms with range (0, 100) GeV/c and 50 bins.

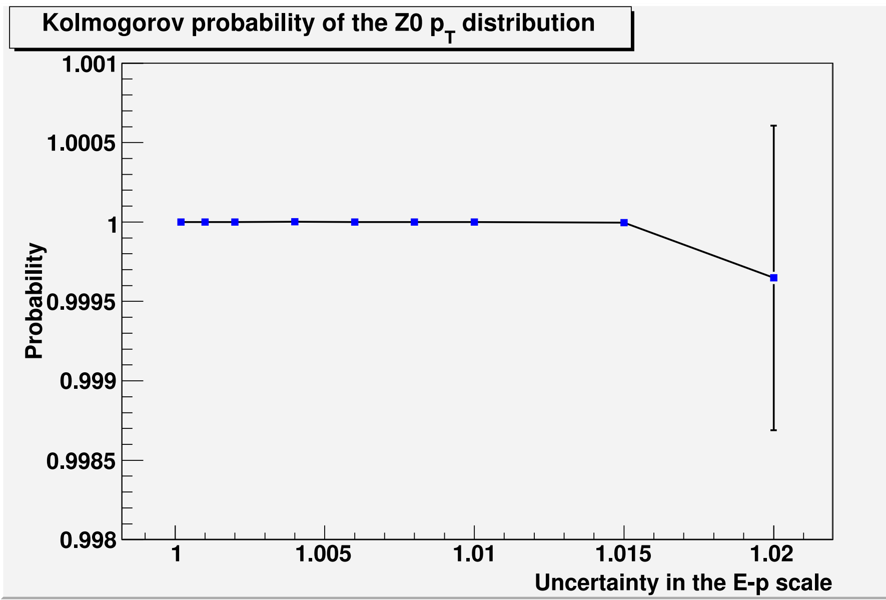

Figure 6.19: Kolmogorov probability of the Z boson p_T distribution for all investigated values of the E-p scale uncertainty. It was created by analyzing the histograms with range (0, 100) GeV/c and 100000 bins.

6.2.6 Z boson rapidity distribution

In the end are shown results for the Z boson rapidity distribution. Following figures show dependence of mean value, RMS and Kolmogorov probability on uncertainty of the E-p scale.

Following figures show, that mean value (Figure 6.20) of rapidity distribution remains approximately constant. RMS values (Figure 6.21) slightly decrease for most of investigated values of the E-p scale uncertainty. Kolmogorov probability (Figure 6.22) remains constant and equal to one for all investigated values of the E-p scale uncertainty.

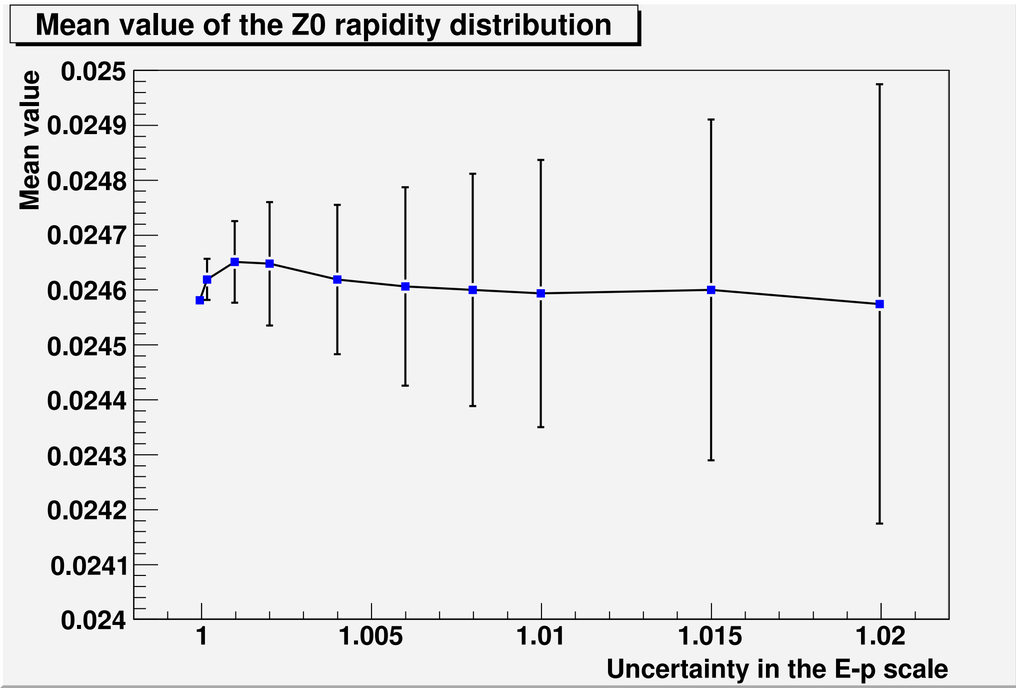

Figure 6.20: Mean value of the Z boson rapidity distribution for all investigated values of the E-p scale uncertainty. It was created by analyzing the histograms with range (-3, 3) and 60 bins.

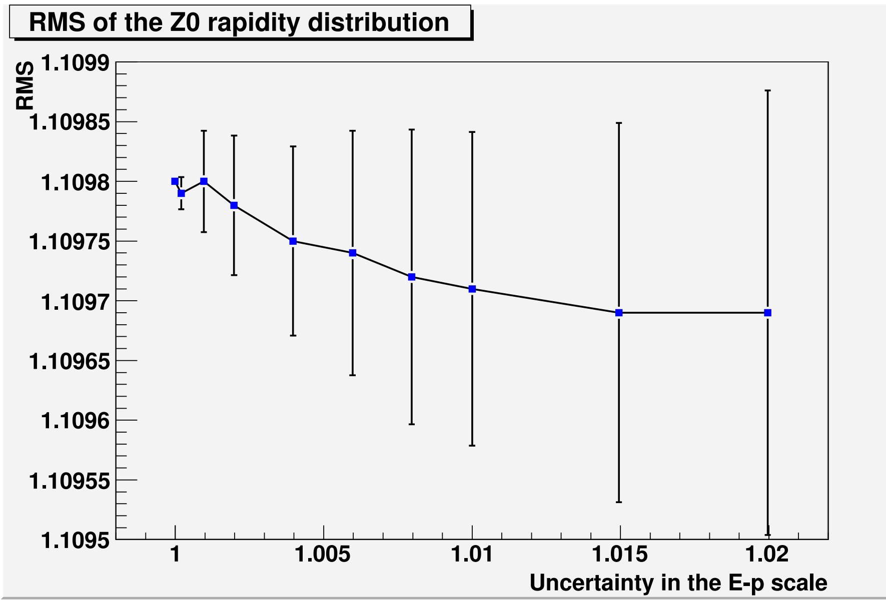

Figure 6.21: RMS of the Z boson rapidity distribution for all investigated values of the E-p scale uncertainty. It was created by analyzing the histograms with range (-3, 3) and 60 bins.

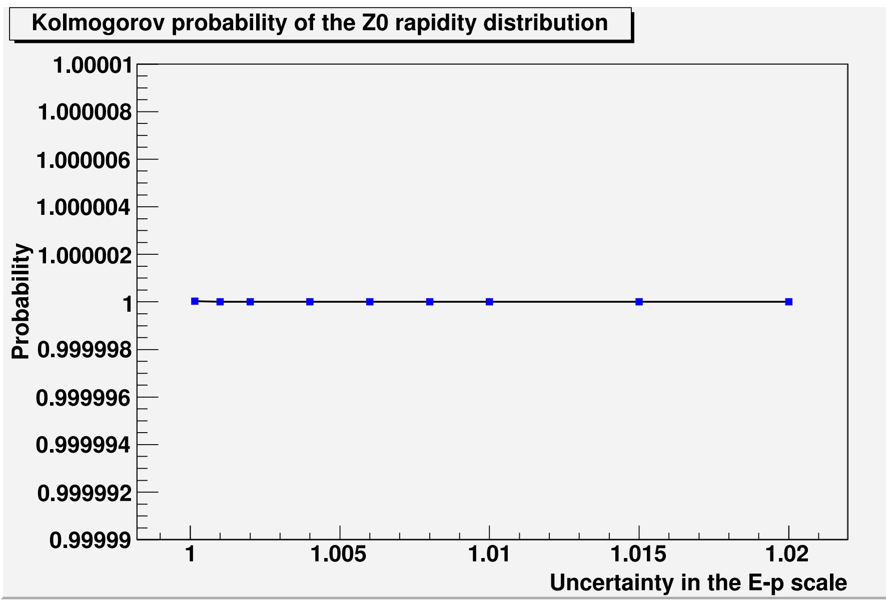

Figure 6.22: Kolmogorov probability of the Z boson rapidity distribution for all investigated values of the E-p scale uncertainty. It was created by analyzing the histograms with range (-3, 3) and 120000 bins.

6.3 Conclusions

Figures 6.5 and 6.6 and Table 6.1 imply, that the most sharp decrease of the number of events happens between the first and the second level of event selection. Investigated interval of E-p scale uncertainty goes from the goal value (0.02 %) to starting value (2 %). Table 6.2 shows, that uncertainty of the E-p scale has almost no effect on the number of events.

Now follow results of Z boson mass distribution fitting. First is shown dependence of fit parameters on the evolution of mass distribution. It starts off by generation and ends with reconstruction. Generated Z boson is created by quark-antiquark annihilation. Then it decays into lepton pair (electron-positron pair). Energy of the lepton pair can be different from energy of generated Z boson because of the final state radiation (after creation of pair, electron and/or positron can emit photon). Then event containing lepton pair is simulated. Electron and positron are reconstructed from simulated response of detector system. Reconstructed Z boson is assembled from fourmomenta of reconstructed electron and reconstructed positron. Figure 6.9 shows that fitted mean value of Z boson mass distribution decreases in similar way both for relativistic Breit-Wigner and Gaussian distribution, but relativistic Breit-Wigner distribution is closer to correct value [9] from generation to reconstruction. FWHM (figure 6.10) increases in similar way both for relativistic Breit-Wigner and Gaussian distribution from generation to reconstruction. Graph depicted on figure 6.11 shows that relativistic Breit-Wigner distribution is better for generated entities, but reconstructed entities are fitted better by Gaussian distribution. It is because Breit-Wigner distribution is inserted into the generator as Z boson mass distribution. Gaussian distribution describes reconstructed entities better because of statistical character of reconstruction process.

The rest of analysing part is dedicated to influence of the uncertainty of the E-p scale on mass, p_T and rapidity distributions of the Z boson. Figure 6.12 implies, that relativistic Breit-Wigner distribution is closer to correct value of Z boson mass for all investigated values of the E-p scale uncertainty. Figure 6.13 shows, that FWHM of both relativistic Breit-Wigner and Gaussian distribution increases for all investigated values of the E-p scale uncertainty. Figure 6.14 shows, that Gaussian distribution fits reconstructed mass of Z boson better than relativistic Breit-Wigner distribution for all investigated values of the E-p scale uncertainty. Result from figures 6.15 and 6.16 implies, that Kolmogorov probability drops with E-p scale uncertainty, thus distribution with high uncertainty of the E-p scale does not seem to come from the same parent distribution.

From figure 6.17 results very slow increase of the mean value of p_T distribution for most of investigated values of the E-p scale uncertainty. RMS values decrease also very slowly for most of investigated values of the E-p scale uncertainty as depicted on figure 6.18. Figure 6.19 shows, that Kolmogorov probability remains equal to one for almost all investigated values of the E-p scale uncertainty.

From figure 6.20 is visible, that mean value of rapidity distribution remains approximately constant. RMS values slightly decrease for most of investigated values of the E-p scale uncertainty as depicted on figure 6.21. Figure 6.22 shows, that Kolmogorov probability remains equal to one for all investigated values of the E-p scale uncertainty.

Mass distributions with range (60, 200) GeV/c^2 (Figure 6.15) are identical at the confidence level 95 % up to the value of the E-p scale uncertainty 0.4 %. Mass distributions with range (88.5, 94) GeV/c^2 (Figure 6.16) are identical at the confidence level 95 % up to the value of the E-p scale uncertainty 0.6 %. p_T distribution with range (0, 100) GeV/c (Figure 6.19) and rapidity distribution with range (-3, 3) (Figure 6.22) are identical at the confidence level 95 % for all investigated values of the E-p scale uncertainty.

Bibliography

[1] The ATLAS Experiment at the CERN Large Hadron Collider, atl-com-phys-2007-087

[2] Lucia Di Ciaccio, Corinne Goy, Stéphane Jézéquel,Robert Zitoun, "Early extraction of the $Z \longrightarrow e^+e^-$ signal using the Atlas detector", atl-phys-int-2007-006

[3] O.Bruning, P.Collier, P.Lebrun, S.Myers, R.Ostojic, J.Poole and P.Proudlock, "LHC design report. Vol. I: The LHC main ring," CERN-2004-003-V-1

[4] M.Benedikt, P.Collier, V.Mertens, J.Poole and K.Schindl, "LHC Design Report. 3. The LHC injector chain," CERN-2004-003-V-3

[5] ATLAS Collaboration, "ATLAS: Detector and physics performance technical design report. Volume 1," CERN-LHCC-99-14

[6] ATLAS Collaboration, "ATLAS detector and physics performance. Technical design report. Vol. 2," CERN-LHCC-99-15

[7] E. Tsesmelis, "Commissioning The Lhc Physics Programme," *Prepared for 3rd LHC Project Workshop: 15th Chamonix Workshop, Chamonix, Divonne-les-Bains, Switzerland, 23-27 Jan 2006*

[8] J. M. Campbell, J. W. Huston and W. J. Stirling, "Hard interactions of quarks and gluons: A primer for LHC physics," Rept. Prog. Phys. **70** (2007) 89 [arXiv:hep-ph/0611148].

[9] W.-M. Yao et al., J. Phys. G, 33, 1(2006)

[10] J.Hladký, "Detektory, systémy detektorů a aparatury pro fyziku částic", lecture text

[11] I.Štoll,"Mechanika", Vydavatelství ČVUT, 1995

[12] http://root.cern.ch/

[13] http://root.cern.ch/root/html/TMath.html

[14] http://gridui02.usatlas.bnl.gov:25880/server/pandamon/query?taskname=7539&overview=taskinfo